General Disclaimer

One or more of the Following Statements may affect this Document

- This document has been reproduced from the best copy furnished by the organizational source. It is being released in the interest of making available as much information as possible.

- This document may contain data, which exceeds the sheet parameters. It was furnished in this condition by the organizational source and is the best copy available.

- This document may contain tone-on-tone or color graphs, charts and/or pictures, which have been reproduced in black and white.

- This document is paginated as submitted by the original source.

- Portions of this document are not fully legible due to the historical nature of some of the material. However, it is the best reproduction available from the original submission.

MLS AIRBORNE ANTENNA RESEARCH

C. L. Yu and W. D. Burnside

The Ohio State University

ElectroScience Laboratory

Department of Electrical Engineering
Columbus, Ohio 43212

NOV 19
RECEIVED
NASA STI FACILITY
INPUT BRANCH

NOTICES

When Government drawings, specifications, or other data are
used for any purpose other than in connection with a definitely
related Government procurement operation, the United States
Government thereby incurs no responsibility nor any obligation
whatsoever, and the fact that the Government may have formulated,
furnished, or in any way supplied the said drawings, specifications,
or other data, is not to be regarded by implication or otherwise as
in any manner licensing the holder or any other person or corporation,
or conveying any rights or permission to manufacture, use, or sell
any patented invention that may in any way be related thereto.

MLS AIRBORNE ANTENNA RESEARCH

C. L. Yu and W. D. Burnside

SEMI-ANNUAL REPORT 2902-22

May 1975

Grant NGL 36-003-138

ABSTRACT

The geometrical theory of diffraction was used to analyze the elevation plane pattern of on-aircraft antennas. The radiation patterns for basic elements (infinitesimal dipole, circumferential and axial slot) mounted on fuselage of various aircrafts with or without radome included were claculated and compared well with experimental results. Error phase plots were also presented. The effects of radiation patterns and error phase plots on the polarization selection for the MLS airborne antenna were discussed.

CONTENTS

iii

I. INTRODUCTION

For the past few years, theoretical solutions for the evaluation, location, and design of fuselage mounted on-aircraft antennas based on pattern performance have been developed at the ElectroScience Laboratory. These numerical solutions have been tested and verified wherever applicable for a wide variety of aircraft and spacecraft antenna problems. The solutions are based on the radiation patterns of the three basic infinitesimal elements (axial slot, circumferential slot, and monopole) which can be used to simulate an arbitrary fuselage mounted antenna aperture distribution. To illustrate this point the solutions have provided the radiation patterns of a circular waveguide antenna mounted on a space shuttle, of an open ended rectangular waveguide antenna on a KC-135 aircraft, and of an array of monopoles on an F-4. Due to the efficiency with which these numerical solutions provide antenna pattern performance, it is appropriate at this time that they be applied in the evaluation of various antenna problems such as the evaluation of the airborne antennas for the microwave landing system.

One of the main obstacles in the development of the FAA microwave landing system has been the appropriate polarization (horizontal or vertical) of the radiated electromagnetic field. Most of the previous discussions on this matter have been based on the ground effects; however, the airborne antenna is an integral part of the system and might have a definite influence on the polarization discussions. Therefore, a study is being made of the airborne problem in terms of the antenna complexity necessary to achieve the desired coverage for both polarizations. This is both a theoretical and experimental study in that various results are compared in terms of scale model measurements taken at NASA (Langley).

The basic requirement for the airborne antennas involves the forward hemisphere coverage of a forward mounted antenna; whereas, the aft sector is covered by a tail mounted antenna. The forward antenna is the primal antenna in that it is used for landing maneuvers; whereas, the tail mounted antenna is used in a missed approach mode. So this study is primarily concerned with the forward fuselage mounted antenna.

As in any study of this type, it is initiated using a simple model of a basic aircraft neglecting the radome. The antennas initially being the three basic antenna elements. Once this result is verified by scale model measurements, the radome is added to both the analysis and scale models. Again, these results are compared to verify the theoretical solutions. Note that this is a study of fuselage mounted antennas and not antennas mounted behind radomes.

II. THEORETICAL BACKGROUND

The theoretical technique used to analyze the radiation patterns of antennas mounted on aircraft fuselages is the geometrical theory of diffraction. It is a high frequency technique with the only

limitation being that the source and various scattering centers be separated on the order of a wavelength or more. The GTD technique and its extensions [1, 2, 3] have been successfully applied to radiation problems for apertures mounted in perfectly conducting wedge surfaces and smooth convex curved surfaces, including circular and elliptic cylinders, spheres, and spheroids [4]. This technique has been applied to such aircraft as the KC-135 and F-4 with good agreement obtained between calculations and measurements [6]. Consequently, the GTD approach is employed to study the airborne problem in terms of the antenna complexity necessary to achieve the desired coverage for both polarizations.

In most cases, the dominant structural effect in the elevation plane is the profile of the aircraft for fuselage mounted antennas. In order to simulate the wide variety of aircraft profiles, it is desirable to analyze a composite ellipse model. This model consists of two semi-ellipses mounted back-to-back.

One of the nicer features of GTD is that it can be extended to new structures by using the existing solutions available after making certain assumptions. For our case, the solution for slot and monopole antennas mounted on an infinitely long elliptic cylinder can be used to analyze the radiation problem of sources mounted on a composite elliptic cylinder with some modification.

The GTD solutions for the radiated electric field from an infinitesimal slot and monopole antenna mounted on an elliptic cylinder as shown in Fig. 1 are given, neglecting torsional effects, by [3, 4, 7].

A.   **Monopole Case**

Lit Region

(1) $\vec{E} = - \sin \theta_m \, \hat{\theta}_m \, F(source)$

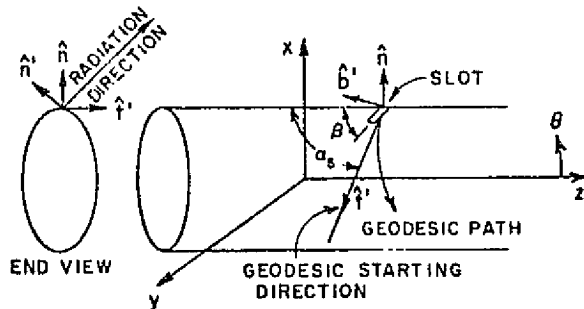**Transition Region**

a) **Lit side**

(2) $\vec{E} = \hat{n} \left\{ 1/2(\sin \theta_m) \, e^{jk\ell} \, g^* \left[- \int \left(\frac{k}{2\rho_g^2(\ell)} \right)^{1/3} d\ell \right] \right\} \cdot F(tangent)$

b) **Shadow side**

(3) $\vec{E} = \hat{n} \left\{ 1/2 \sqrt{\frac{d\psi_0}{d\psi}} \, e^{-jk\ell} \, g^* \left[\int \left(\frac{k}{2\rho_g^2(\ell)} \right)^{1/3} d\ell \right] \right\} \cdot F(tangent)$

2
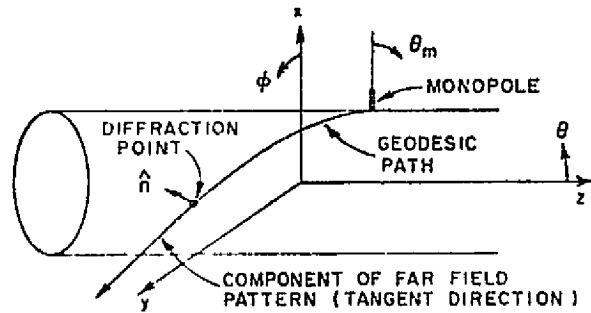
Fig. 1. Geometry of antennas mounted on an infinitely long elliptic cylinder.

Deep Shadow Region

$$(4) \qquad \vec{E} = \sum_j \hat{n}_j \, E_j^h \, F_j \quad \text{(tangent)}$$

B. Slot Case

Lit Region

$$(5) \qquad \vec{E} = [(\hat{e}_1 \sin \beta - \hat{e}_2 \cos \beta) \cdot (\hat{b}'\hat{n}' + \hat{t}'\hat{b}'\cos\theta_m)] \cdot F(\text{source})$$

3

Transition Region

a) Lit side

$$(6) \quad \vec{E} = \left\{ \hat{n} \left[1/2 \; e^{jk\ell} \; g^* \left(-\int \left(\frac{k}{2\rho_g^2(\ell)} \right)^{1/3} d\ell \right) \sin(\alpha_s + \beta) \right] + \right.$$

$$\left. \hat{b} \left[j/2 \; e^{jk\ell} \; \vec{g}^* \left(-\int \left(\frac{k}{2\rho_g^2(\ell)} \right)^{1/3} d\ell \right) \left(\frac{2}{k\rho_g} \right)^{1/3}_{\text{at source}} \cos(\alpha_s + \beta) \right] \right\}$$

$$\cdot \; F(\text{tangent})$$

b) Shadow side

$$(7) \quad \vec{E} = \left\{ \hat{n} \left[1/2 \; \sqrt{\frac{d\psi_o}{d\psi}} \; e^{-jk\ell} \; g^* \left(\int \left(\frac{k}{2\rho_g^2(\ell)} \right)^{1/3} d\ell \right) \sin(\alpha_s - \beta) \right] + \right.$$

$$\left. \hat{b} \left[-j/2 \sqrt{\frac{d\psi_o}{d\psi}} \; e^{-jk\ell} \; \vec{g}^* \left(\int \left(\frac{k}{2\rho_g^2(\ell)} \right)^{1/3} d\ell \right) \left(\frac{2}{k\rho_g} \right)^{1/3}_{\text{at source}} \cos(\alpha_s - \beta) \right] \right\}$$

$$\cdot \; F(\text{tangent})$$

Deep Shadow Region

$$(8) \quad \vec{E} = \sum_j \left[\hat{n}_j \; E_j^h \; \sin(\alpha_s - \beta) + \hat{b}_j \; E_j^s \; \cos(\alpha_s - \beta) \right] F_j(\text{tangent})$$

where

$$E^h = \sqrt{\frac{d\psi_o}{d\psi}} \; \sum_{m=0}^{1} D_m^h \; L_m^h \; e^{-\int \gamma_m^h(\ell) d\ell}$$

$$E^s = \sqrt{\frac{d\psi_o}{d\psi}} \; \sum_{m=0}^{1} D_m^s \; L_m^s \; e^{-\int \gamma_m^s(\ell) d\ell}$$

4

$g^*(\ )$, $\tilde{g}^*(\ )$ = complex conjugates of the Fock functions[1].

$\hat{n}$, $\hat{b}$, $\hat{t}$ = the normal, binormal, and tangent unit vectors to the surface.

$F(\ )$ = phase factor to refer the phase to the center of the coordinate system.

$\sqrt{d\psi_0/d\psi}$ = is the spread factor and equals unity for this case[1].

ρ_g, ρ_t = longitudinal and transverse radii of curvature.

Note that the superscripts h and s indicate the hard and soft boundary conditions, respectively. The launch coefficients are given by [1]

$$L_m^h = \left[\pi e^{j\frac{\pi}{12}} D_m^h \left(\frac{2}{k\rho_g}\right)^{1/3} A_i(-\bar{q}_m) \right] \text{ at the source}$$

$$L_m^s = \left[\pi e^{-j\frac{\pi}{12}} D_m^s \left(\frac{2}{k\rho_g}\right)^{2/3} A_i'(-q_m) \right] \text{ at the source}$$

where D_m is defined in Table I. The subscript m refers to the mth mode of the boundary layer surface wave. Thus, γ_m is the propagation constant for the mth mode surface wave such that $\gamma_m = \alpha_m + jk$ where α_m is defined in Table I. The incremental arc length along the geodesic path is expressed by $d\ell$. The summation over "j" in the shadow region indicates that several terms can contribute in that region.

One must first find an efficient solution for the geodesic paths on the elliptic cylinder surface in order to analyze this problem successfully using GTD. A preferred coordinate system for the elliptic cylinder is illustrated in Fig. 2 and defined by

$$x = d \cosh u \cos v = a_f \cos v$$

(9) $$y = d \sinh u \sin v = b_f \sin v$$

$$z = z$$

TABLE I

GENERALIZED DIFFRACTION COEFFICIENTS AND ATTENUATION CONSTANTS

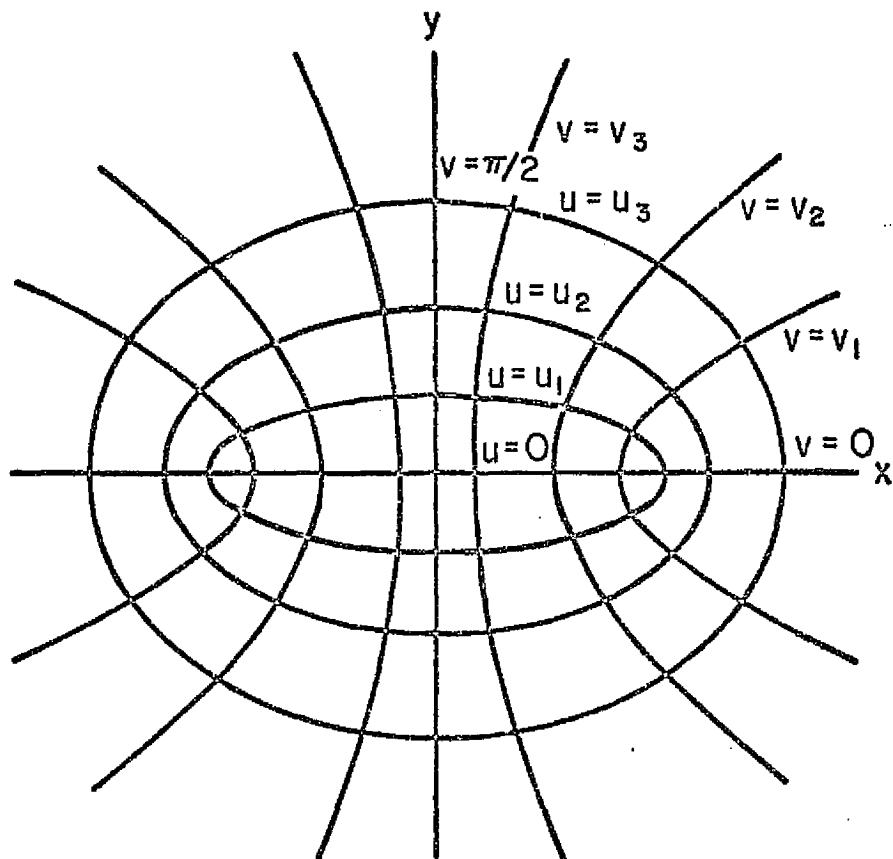| Surface	Square of Diffraction Coefficient D_m^2 = (Column A) · (Column B)		Attenuation Constant α_m = (Column C) · (Column D)	
	A. Keller's Result	B. Correction Terms	C. Keller's Result	D. Correction Terms
Soft Acoustic and Soft DN	$\dfrac{e^{-1/2} z^{-5/6} \rho_g^{1/3} e^{-j\pi/12}}{k^{1/6} \{Ai'(-\alpha_m)\}^2}$	$1 + \left(\dfrac{2}{k\rho_g}\right)^{2/3} \alpha_m\left(\dfrac{1}{30} + \dfrac{\rho_g}{4\rho_{tn}} + \dfrac{\rho_g\tilde{\rho}_g}{180}\right) e^{-j\pi/3}$	$\dfrac{\alpha_m}{\rho_g} e^{j\pi/6}\left(\dfrac{k\rho_g}{2}\right)^{1/3}$	$1 + \left(\dfrac{2}{k\rho_g}\right)^{2/3} \alpha_m\left(\dfrac{1}{60} - \dfrac{2}{45}\cdot\rho_g\tilde{\rho}_g + \dfrac{4}{135}\cdot\tilde{\rho}_g^2\right) e^{-j\pi/3}$
Hard Acoustic	$\dfrac{e^{-1/2} z^{-5/6} \rho_g^{1/3} e^{-j\pi/12}}{k^{1/6}\,\bar{q}_m\{Ai(-\bar{q}_m)\}^2}$	$1 + \left(\dfrac{2}{k\rho_g}\right)^{2/3}\left(\bar{q}_m\left(\dfrac{1}{30} + \dfrac{\rho_g}{4\rho_{tn}} + \dfrac{\rho_g\tilde{\rho}_g}{180}\right) - \dfrac{1}{\bar{q}_m}\left(\dfrac{1}{10} + \dfrac{\rho_g}{4\rho_{tn}} - \dfrac{\rho_g\tilde{\rho}_g}{60}\right)\right) e^{-j\pi/3}$	$\dfrac{\bar{q}_m}{\rho_g} e^{j\pi/6}\left(\dfrac{k\rho_g}{2}\right)^{1/3}$	$1 + \left(\dfrac{2}{k\rho_g}\right)^{2/3}\left(\bar{q}_m\,\dfrac{1}{60} - \dfrac{2}{45}\cdot\rho_g\tilde{\rho}_g + \dfrac{4}{135}\cdot\tilde{\rho}_g^2\right) + \dfrac{1}{\bar{q}_m^2}\left(\dfrac{1}{10} + \dfrac{\rho_g}{4\rho_{tn}} - \dfrac{\rho_g\tilde{\rho}_g}{60} + \dfrac{\tilde{\rho}_g^2}{90}\right)\right) e^{-j\pi/3}$
Hard DN		$1 + \left(\dfrac{2}{k\rho_g}\right)^{2/3}\left(\bar{q}_m\left(\dfrac{1}{30} + \dfrac{\rho_g}{4\rho_{tn}} + \dfrac{\rho_g\tilde{\rho}_g}{180}\right) - \dfrac{1}{\bar{q}_m}\left(\dfrac{1}{10} - \dfrac{\rho_g}{4\rho_{tn}} - \dfrac{\rho_g\tilde{\rho}_g}{60}\right)\right) e^{-j\pi/3}$		$1 + \left(\dfrac{2}{k\rho_g}\right)^{2/3}\left(\bar{q}_m\left(\dfrac{1}{60} - \dfrac{2}{45}\cdot\rho_g\tilde{\rho}_g + \dfrac{4}{135}\cdot\tilde{\rho}_g^2\right) + \dfrac{1}{\bar{q}_m^2}\left(\dfrac{1}{10} - \dfrac{\rho_g}{4\rho_{tn}} - \dfrac{\rho_g\tilde{\rho}_g}{60} + \dfrac{\tilde{\rho}_g^2}{90}\right)\right) e^{-j\pi/3}$

Fig. 2. Diagram showing the elliptic cylinder coordinate system.

6

where 2d is the distance between the foci of the ellipse. Note that for $u = u_f$, where $u_f = \tanh^{-1}(b_f/a_f)$, the above equations define an elliptical surface for $0 \leq v < 2\pi$. Thus, the general shape of the elliptic surface is expressed by u_f, and its dimensions are defined by d.

Using the calculus of variations, the geodesic paths on an elliptical surface are given by

$$(10) \qquad z = \frac{C}{\sqrt{1-C^2}} \int_{v_i}^{v_f} \sqrt{a_f^2 \sin^2 v + b_f^2 \cos^2 v} \; dv \qquad .$$

Note that v_i and v_f, respectively, are the initial and final values of v along a given geodesic path. If one defines the geodesic starting direction by the angle (α_s) as shown in Fig. 1, then $C = -\cos \alpha_s$. The advantage of this geodesic solution lies in the fact that the integral can be quickly evaluated using numerical techniques. The important parameters of this problem are listed below:

$$z = \frac{-\cos \alpha_s}{|\sin \alpha_s|} \int_{v_i}^{v_f} \sqrt{a_f^2 \sin^2 v + b_f^2 \cos^2 v} \; dv \qquad \text{(geodesic equation)}$$

$$\ell = \frac{1}{|\sin \alpha_s|} \int_{v_i}^{v_f} \sqrt{a_f^2 \sin^2 v + b_f^2 \cos^2 v} \; dv \qquad \text{(arc length)}$$

$$\hat{e}_1 = \frac{-a_f \sin v \, \hat{x} + b_f \cos v \, \hat{y}}{\sqrt{a_f^2 \sin^2 v + b_f^2 \cos^2 v}} \left.\begin{matrix} \\ \\ \\ \\ \end{matrix}\right\} \text{(curvilinear coordinates)}$$

$$\hat{e}_2 = \hat{z}$$

$$\hat{t} = \sin \alpha_s \, \hat{e}_1 - \cos \alpha_s \, \hat{e}_2 \qquad \text{(unit tangent vector)}$$

$$\hat{n} = \frac{b_f \cos v \, \hat{x} + a_f \sin v \, \hat{y}}{\sqrt{a_f^2 \sin^2 v + b_f^2 \cos^2 v}} \qquad \text{(unit normal vector)}$$

$$\hat{b} = \hat{t} \times \hat{n} = -\cos \alpha_s \, \hat{e}_1 - \sin \alpha_s \, \hat{e}_2 \qquad \text{(unit binormal vector)}$$

7

$$\rho_g = \frac{(a_f^2 \sin^2 v + b_f^2 \cos^2 v)^{3/2}}{a_f b_f \sin^2 \alpha_s}$$

(longitudinal radius of curvature)

Using the above relations, one can employ Eqs. (1-8) to determine the total radiated fields.

In order to extend the above solutions to our composite elliptic cylinder model, it is assumed that no diffractions occur from the junction lines of the two ellipses. This assumption is justified since these junctions are non-existent in the actual aircraft profile. Note that the GTD solution in the lit region does not depend on the surface parameters in that it is assumed the source is mounted on an infinite ground plane tangent to the surface at the source point. On the other hand, the transition and deep-shadow region solutions are modified due to their dependence upon the surface parameters. This modification simply requires that one use $a_f = a$ for rays traveling to the right of the junction and $a_f = a'$ for rays traveling to the left of the junction. The parameters a and a' are illustrated in Fig. 3b.

This model is, now, applied to analyze the elevation plane radiation patterns for MLS antenna systems mounted on the space shuttle. Since the antennas of interest are located on the fuselage and along the center line, the most significant effects on the pattern result from the surface profile near the antenna. The structure used to simulate the $1/35^{th}$ scale model of the space shuttle as shown in Fig 3 consists of a 60" by 2.55" right semi-ellipse and an 12.5" by 2.55" left semi-ellipse. The elevation patterns calculated using a short monopole and KA-band waveguide mounted on the fuselage are shown in Figs. 4 to 6. The KA-band waveguide aperture fields are simulated in our model by an array of infinitesimal elements as shown in Fig. 7. The experimental results were taken at NASA (Langley). Both theoretical and experimental data show good agreement. The figures, also, indicate that vertical polarization might have better coverage than horizontal polarization for the antenna location considered.

In the previous analysis, the effect of the aircraft radome was neglected. In order to simulate a fuselage with radome, a truncated composite elliptic cylinder model as shown in Fig. 8 is adopted. This is due to the fact that the dielectric constant of most aircraft radomes is close to that of free space. Before one proceeds to solve this problem, careful consideration allows him to convert it into a simpler problem. With the fact that a slot or monopole radiating in the presence of a composite elliptic cylinder can be considered as an antenna itself, the present problem can be reduced to the radiation problem of an equivalent antenna mounted on a wedge type structure as shown in Fig. 9. This equivalent antenna radiates the same pattern as that of a slot or monopole mounted on our previous model without
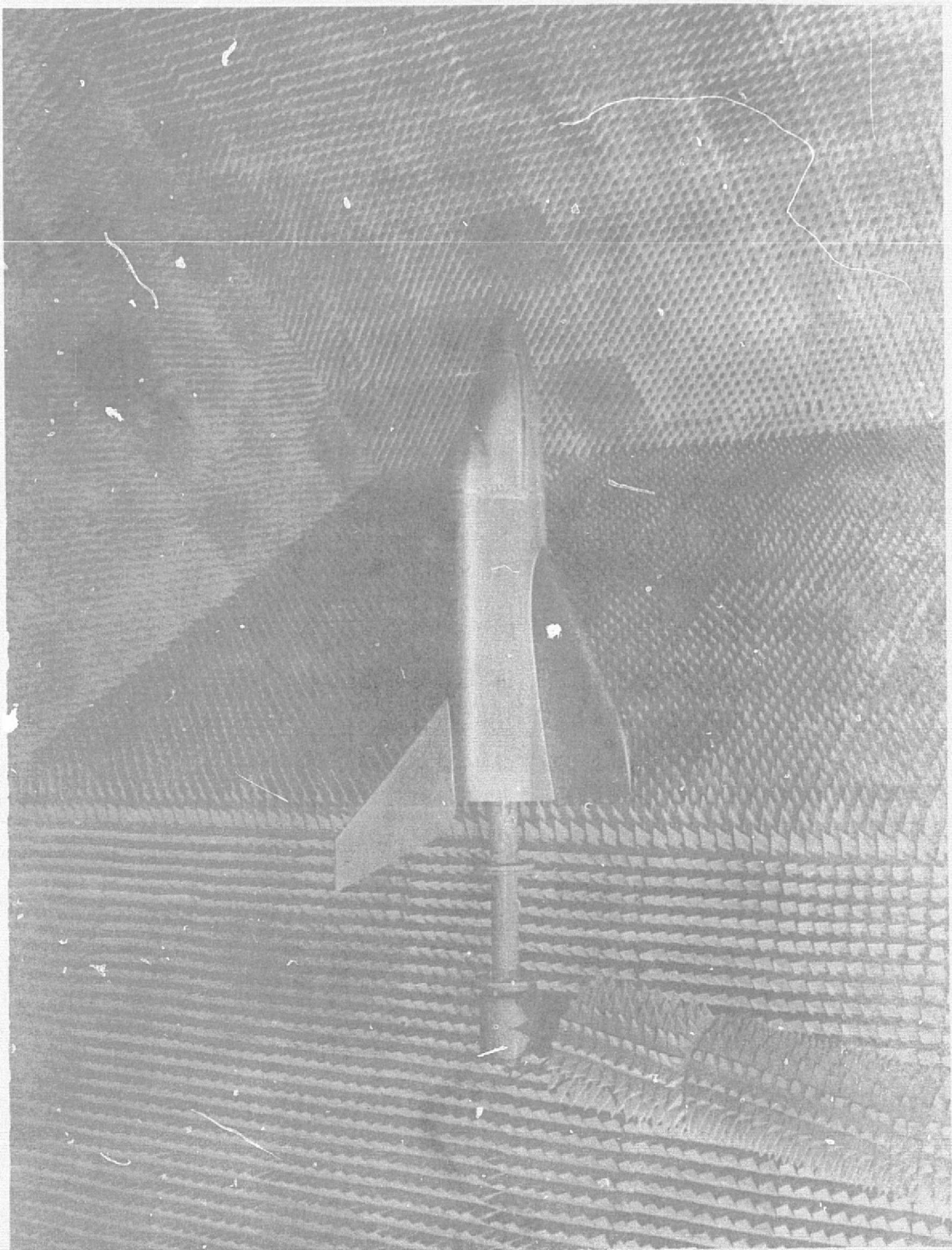
8

Fig. 3a. Scale model (1/35) of Space Shuttle in
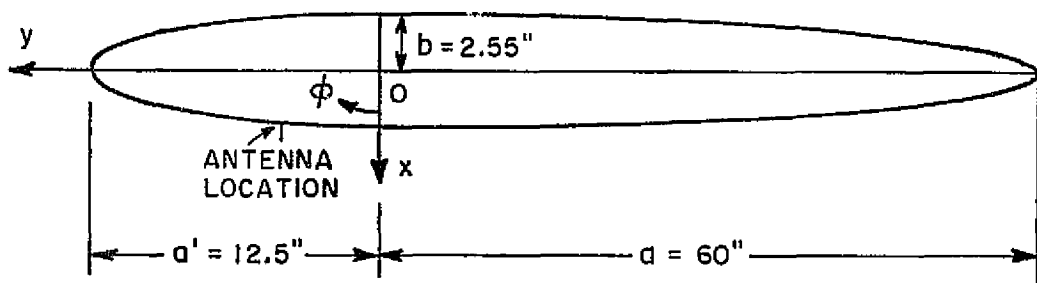Anechoic Chamber at NASA, Langley Center.

Fig. 3b.   Theoretical model of 1/35th scale model of
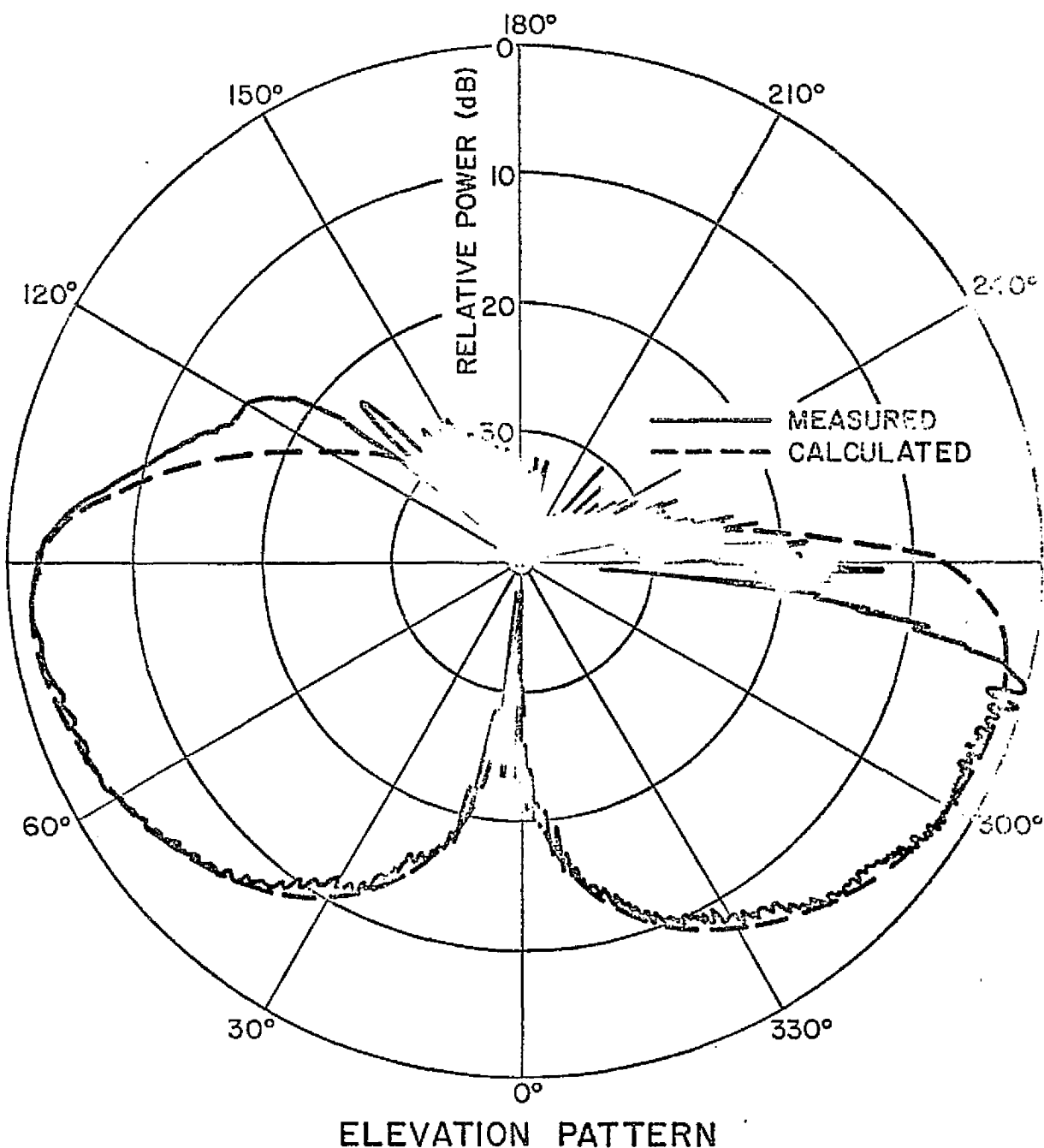   space shuttle.

ELEVATION PATTERN

Fig. 4. Elevation pattern of monopole on a 1/35th scale model of space shuttle (radome being excluded).
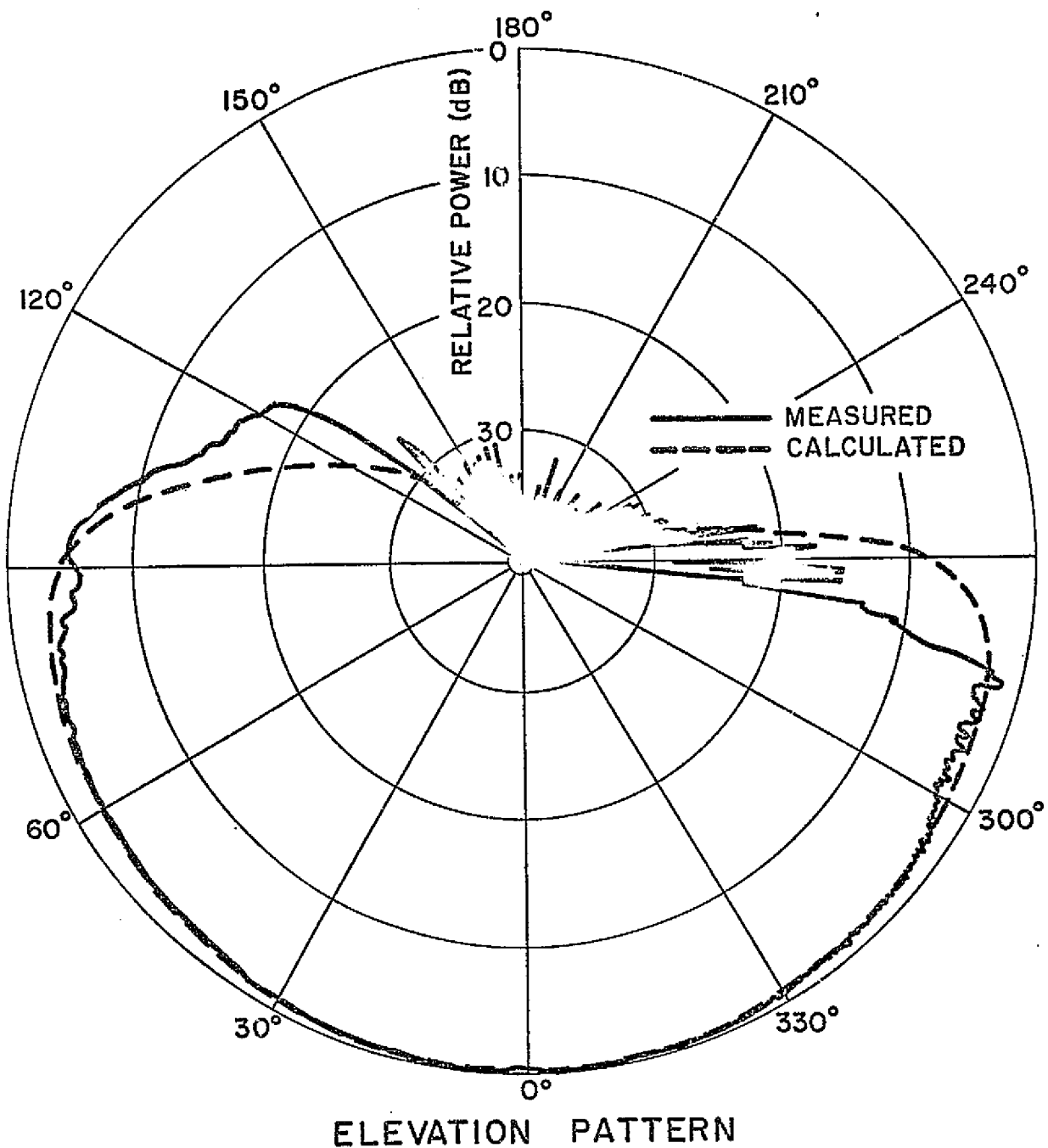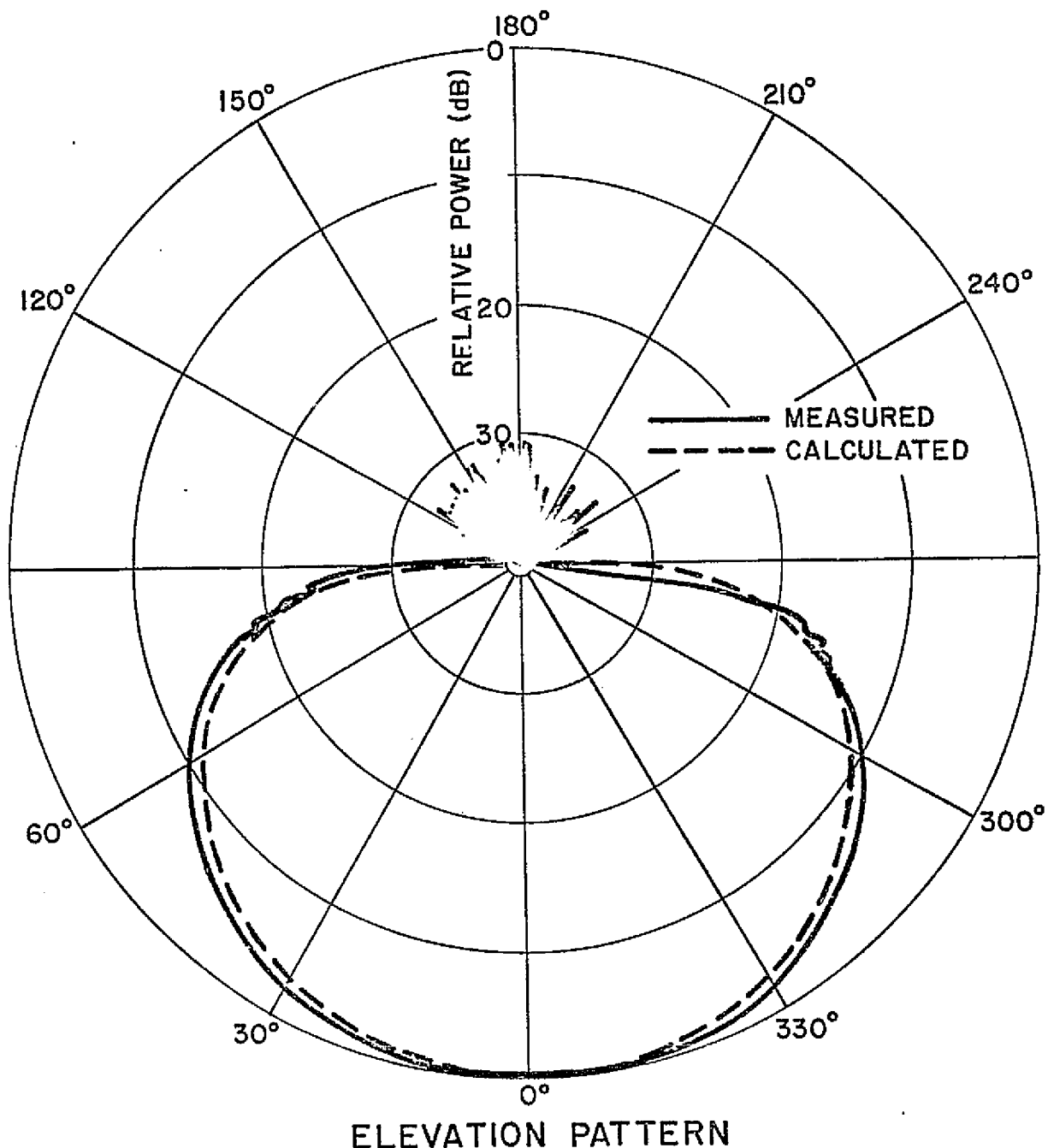
11

VERTICAL POL.
WAVEGUIDE

SPACE SHUTTLE
WITHOUT RADOME

ELEVATION PATTERN

Fig. 5. Elevation pattern of circumferential slot
on a 1/35th scale model of space shuttle
(radome being excluded).

Fig. 6. Elevation pattern of axial slot on a 1/35th
scale model of space shuttle (radome being
excluded).
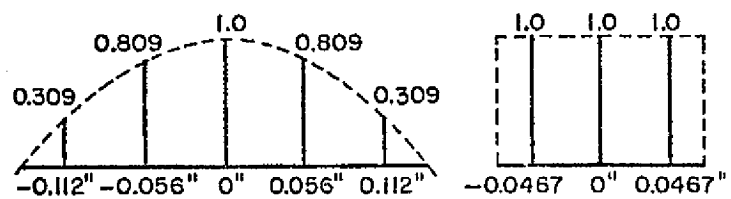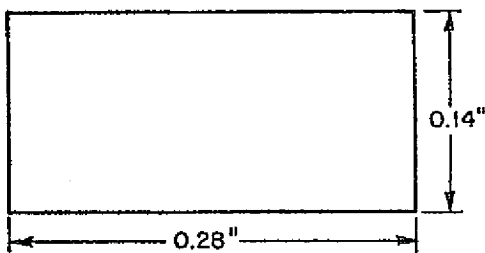
Fig. 7. Approximation of an open-end waveguide by an array
of 5 infinitesimal broad wall elements with different
weights and an array of 3 infinitesimal narrow wall
elements with uniform weight.
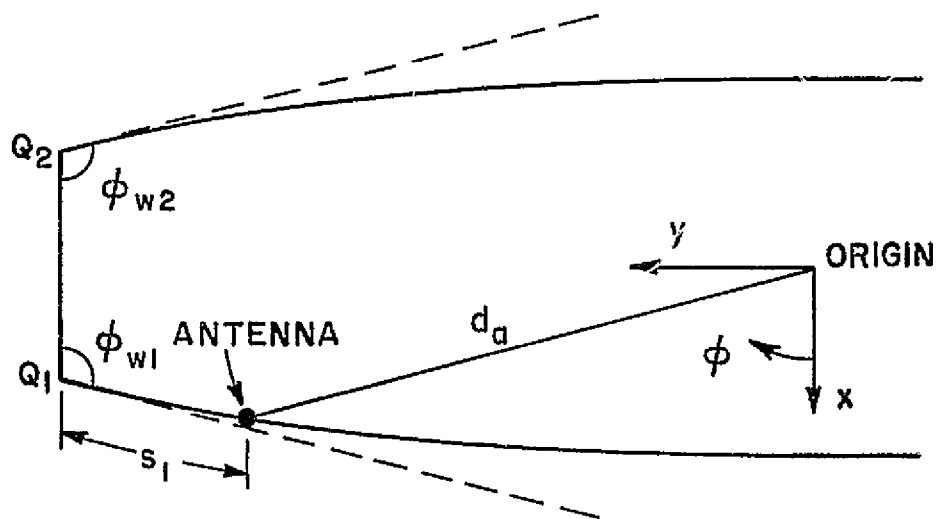
Fig. 8. Truncated composite ellipse as simulation of
fuselage with radome included.
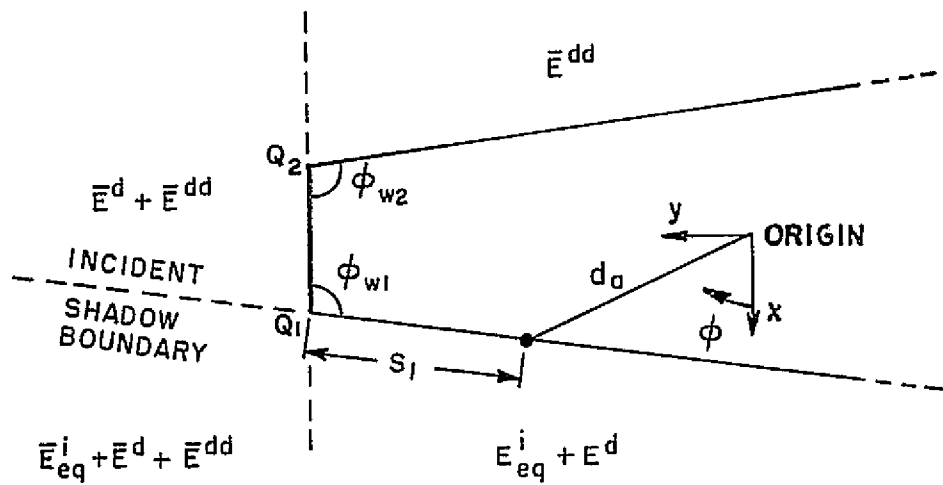
Fig. 9. Total field distribution.

the radome considered. The wedges are formed and defined by the tangent planes at the discontinuities Q_1 and Q_2. Thus, the radiation problem of a fuselage model with a radome included becomes a simple wedge diffraction problem, and can be solved using standard GTD techniques. When the electromagnetic field radiated by this equivalent source is incident on edge 1 as shown in Fig. 9, diffraction occurs. The singly diffracted field can be written as [8]

$$(11) \qquad \bar{E}^d \sim \left[\bar{\bar{D}} \cdot \bar{E}^i + \bar{\bar{d}}_s \cdot \frac{\partial \bar{E}^i}{\partial n} \right] A(s) \, e^{-jks}$$

in which $\bar{\bar{D}}$ is a dyadic diffraction coefficient and $\bar{\bar{d}}_s$ is a dyadic slope diffraction coefficient. The first term inside the bracket is an ordinary diffracted field and the second term is the slope diffracted field. This slope diffracted field compensates for the discontinuities of slope in the geometric optics field across the reflected and shadow boundaries as described in reference [8]. The term [A(s)] in Eq. (12) is the spread factor which describes how the amplitude of the field varies along the diffracted rays, and is given by [9]

$$A(s) = \sqrt{\frac{s'}{s(s'+s)}} \qquad\qquad \text{for spherical wave incidence,}$$

where s' is the distance which the incident ray traverses from the source to edge 1 and s is the distance which the singly diffracted ray traverses from edge 1 to the observation point.

The electric field $\bar{E}^i$ incident at edge 1 is found by assuming an equivalent antenna radiating with the same gain function as that of our previous model and being located a distance s_1 away from the edge 1. The parameter s_1 is the distance which the surface wave, launched by the original source, has travelled before it reaches the point of truncation (edge 1) as shown in Fig. 8 . From Eqs. (3) or (4) and Eqs. (7) or (8), the incident field $\bar{E}^i(Q_1)$ at edge 1 can be obtained, depending upon the direction in which the tangential shedding electric field leaving at edge 1, as

A. Monopole

$$(12) \quad \begin{cases} \bar{E}^i(Q_1) = \hat{n} \left\{ \frac{1}{2} \frac{\overline{d\psi_0}}{d\psi} \frac{e^{-jks_1}}{s_1} \quad g^* \left[\int \left(\frac{k}{2\rho_g^2(\ell)} \right)^{1/3} d\ell \right] \right\} \\ \\ \\ \bar{E}^i(Q_1) = \sum_j \hat{n}_j \, E_j^h(s_1) \end{cases}$$

transition region

shadow region

16

B. Slot case

$$(13) \qquad \bar{E}^i(Q_1) = \left\{ \hat{n} \left[\frac{1}{2}\sqrt{\frac{d\psi_0}{d\psi}} \; \frac{e^{-jks_1}}{s_1} \; g* \left(\int\!\!\int \left(\frac{k}{2\rho_g^2(\ell)} \right)^{1/3} d\ell \right) \right. \right.$$

$$\left. \cdot \sin(\alpha_s - \beta) \right] + \hat{b} \left[-j/2\sqrt{\frac{d\psi_0}{d\psi}} \; \frac{e^{-jks_1}}{s_1} \right.$$

$$\left. \left. \cdot \tilde{g}* \left(\int \left(\frac{k}{2\rho_g^2(\ell)} \right)^{1/3} d\ell \right) \left(\frac{2}{k\rho_g} \right)^{1/3}_{\text{at source}} \cos(\alpha_s - \beta) \right. \qquad \cdot \right.$$

transition region

$$\bar{E}^i(Q_1) = \sum_j \left[\hat{n}_j \; E_j^h(s_1) \sin(\alpha_s - \beta) + \right.$$

$$\left. \hat{b}_j \; E_j^s(s_1) \cos(\alpha_s - \beta) \right] \qquad\qquad \text{shadow region}$$

By combining Eqs. (11), (12), and (13), the singly diffracted field in the far zone is simply given by

$$(14) \qquad \bar{E}^d \sim \left[\bar{\bar{D}} \cdot \bar{E}^i(Q_1) + \bar{\bar{d}}_s \cdot \frac{\partial \bar{E}^i(Q_1)}{\partial n} \right] \sqrt{s_1} \; \frac{e^{-jks}}{s} \; F()$$

where the distance parameter in the dyadic diffraction coefficients reduces to s_1 for the elevation plane case and F() is the phase factor used to refer the phase to the origin.

In a similar manner, when the singly diffracted field from edge 1 arrives at edge 2, double diffraction occurs. Since the diffracted field is related to the incident field by Eq. (11), the doubly diffracted field at edge 2, then, is given by

$$(15) \qquad \bar{E}^{dd} \sim \left[\bar{\bar{D}} \cdot \bar{E}^d(Q_2) + \bar{\bar{d}}_s \cdot \frac{\partial \bar{E}^d}{\partial n}(Q_2) \right] A(s) \; e^{-jks}$$

where $\bar{E}^d(Q_2)$ is the singly diffracted field at edge 2. From Eq. (11),

17

the incident field $\bar{E}^d(Q_2)$ at edge 2 can be obtained without any difficulty as

$$(16) \qquad \bar{E}^d(Q_2) = \left[\overline{\overline{D}} \cdot \bar{E}^i(Q_1) + \overline{\overline{d}}_s \cdot \frac{\partial \bar{E}^i}{\partial n}(Q_1) \right] \sqrt{\frac{s_1}{s_2(s_1 + s_2)}} \; e^{-jks_2}$$

In the far zone, the spreading factor A(s) reduces to $\sqrt{s_2}/s$. Substituting this result into Eq. (15), the far zone diffracted field from edge 2, then, is given by

$$(17) \qquad \bar{E}^{dd} \sim \left[\overline{\overline{D}} \cdot \bar{E}^d(Q_2) + \overline{\overline{d}}_s \cdot \frac{\partial \bar{E}^d}{\partial n}(Q_2) \right] \sqrt{s_2} \; \frac{e^{-jks}}{s} \; F()$$

Higher order diffractions exist due to the same diffraction mechanism with rays from these two edges interacting with each other; however, the contributions from these higher order diffraction terms are so small compared to single and double diffraction that they can be ignored for our purposes. Hence, the total electric field in far zone is obtained by including the appropriate contributions of the diffracted fields from edge 1 and edge 2 as shown in Fig. 9, and given by

$$(18) \qquad \bar{E}^t = \begin{cases} \bar{E}^i_{eq} + \bar{E}^d + \bar{E}^{dd} & 0 \leq \phi \leq \phi_{w1} \\[2mm] \bar{E}^d + \bar{E}^{dd} & \phi_{w1} < \phi \leq \pi \\[2mm] \bar{E}^{dd} & \pi < \phi \leq 2\pi - \phi_{w2} \\[2mm] \bar{E}^i_{eq} + \bar{E}^d & \pi + \phi_{w1} \leq \phi \leq 2\pi \end{cases}$$

Note that $\bar{E}^i_{eq}$ is the radiated field of the equivalent antenna described above and is given by Eqs. (1) to (8).

Using the previously described solution, the elevation plane patterns for the space shuttle with the radome included are calculated. Figs. 10 to 12 illustrate the radiation patterns for both vertical (monopole and circumferential waveguide) and horizontal (axial waveguide) polarization sources mounted on the fuselage of the 1/35th scale model of the space shuttle with the radome considered. The structure used to simulate the 1/35th scale model consists of a 12.5 by 2.55 right semi-ellipse and an 60.0 by 2.55 left semi-ellipse. The size of the radome is 6.5" and the source is mounted 2" away from the radome.

18

VERTICAL POL.
MONOPOLE
(8 1/2")

SPACE SHUTTLE
WITH RADOME
(6 1/2")
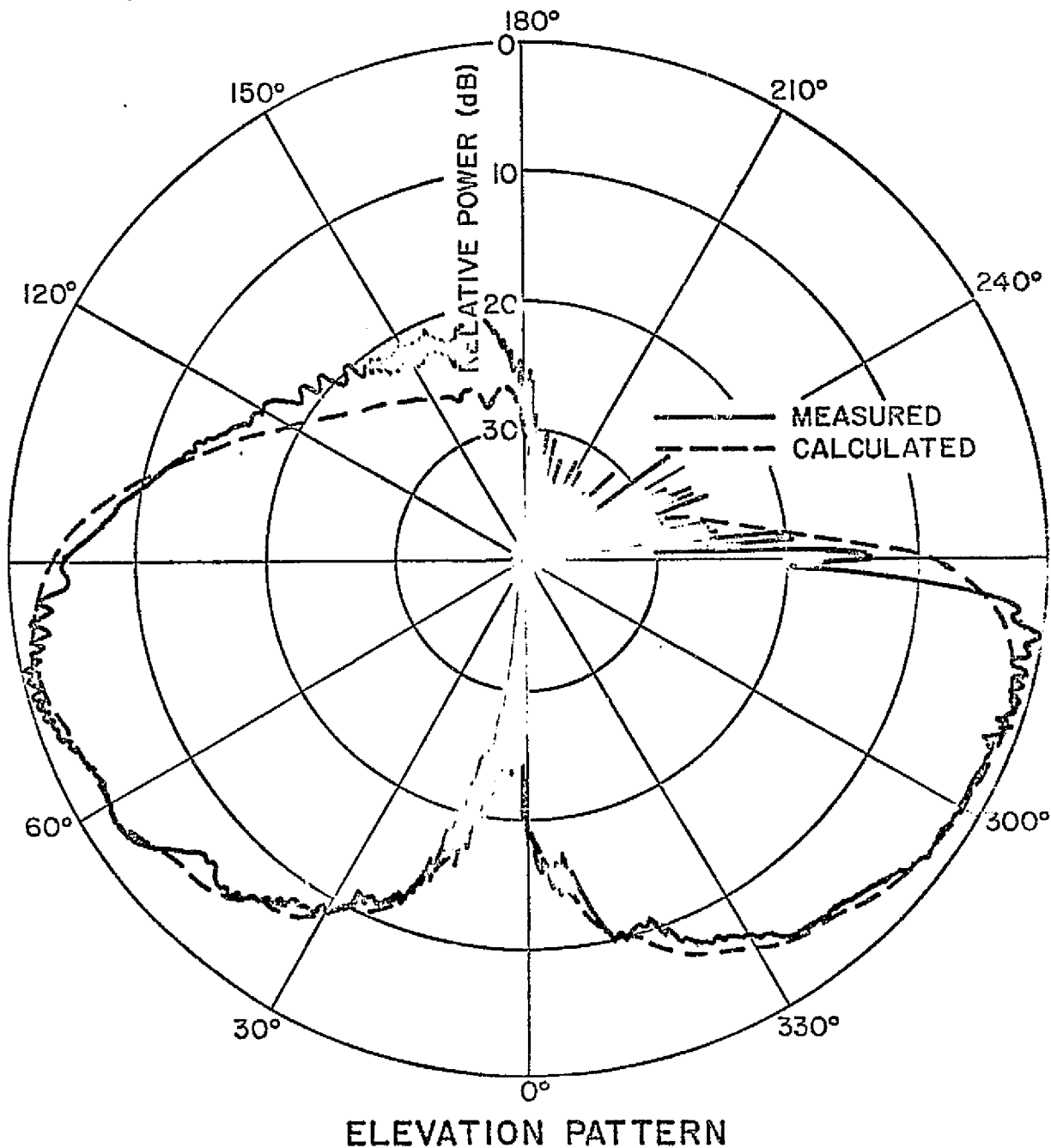
ELEVATION PATTERN

Fig. 10. Elevation pattern of monopole on a 1/35th
scale model of space shuttle (with radome
included).

19

VERTICAL POL.
WAVEGUIDE
(8 ½")

SPACE SHUTTLE
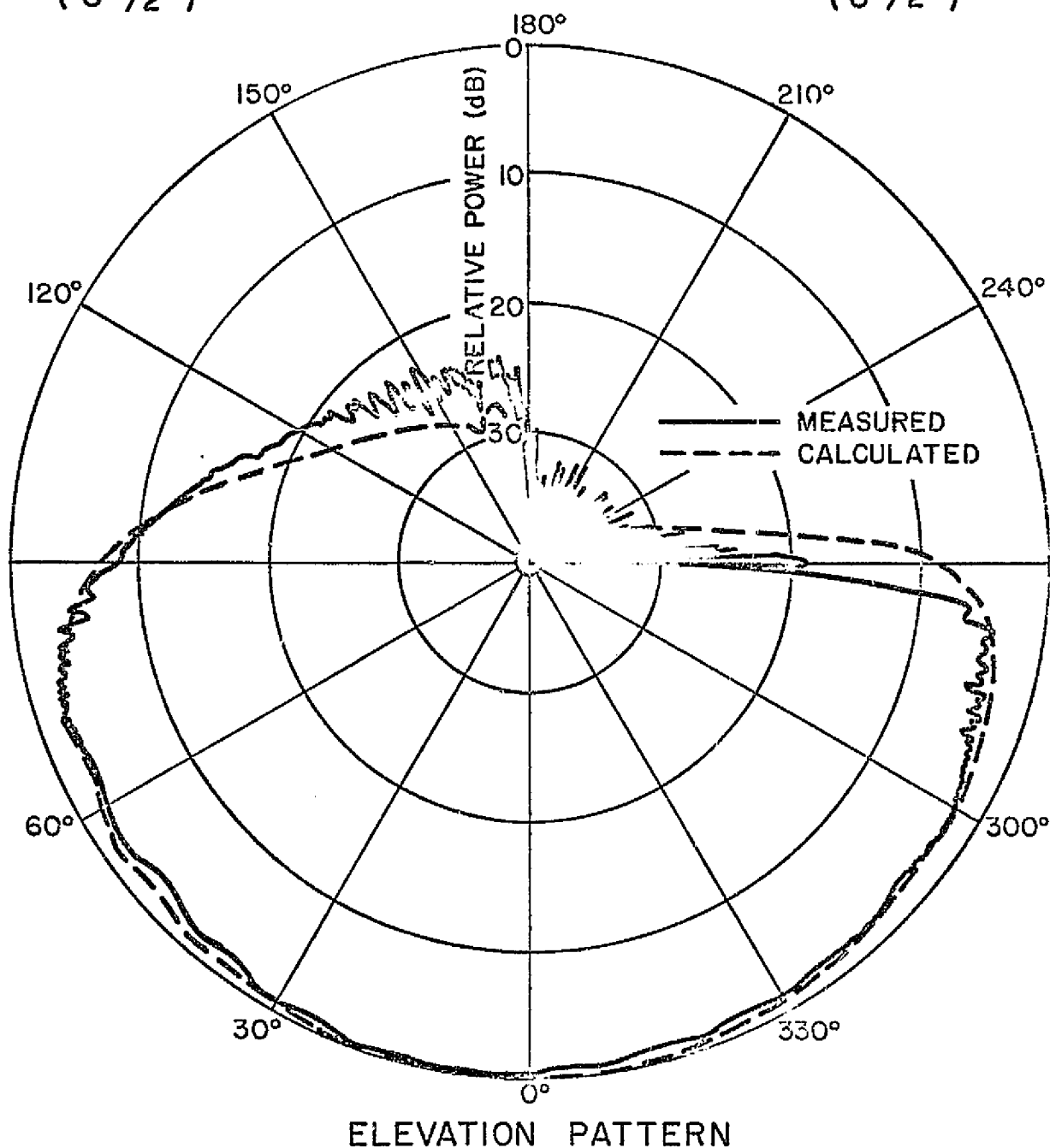WITH RADOME
(6 ½")

ELEVATION PATTERN

Fig. 11. Elevation pattern of circumferential slot
on a 1/35th scale model of space shuttle
(with radome included).

HORIZONTAL POL.
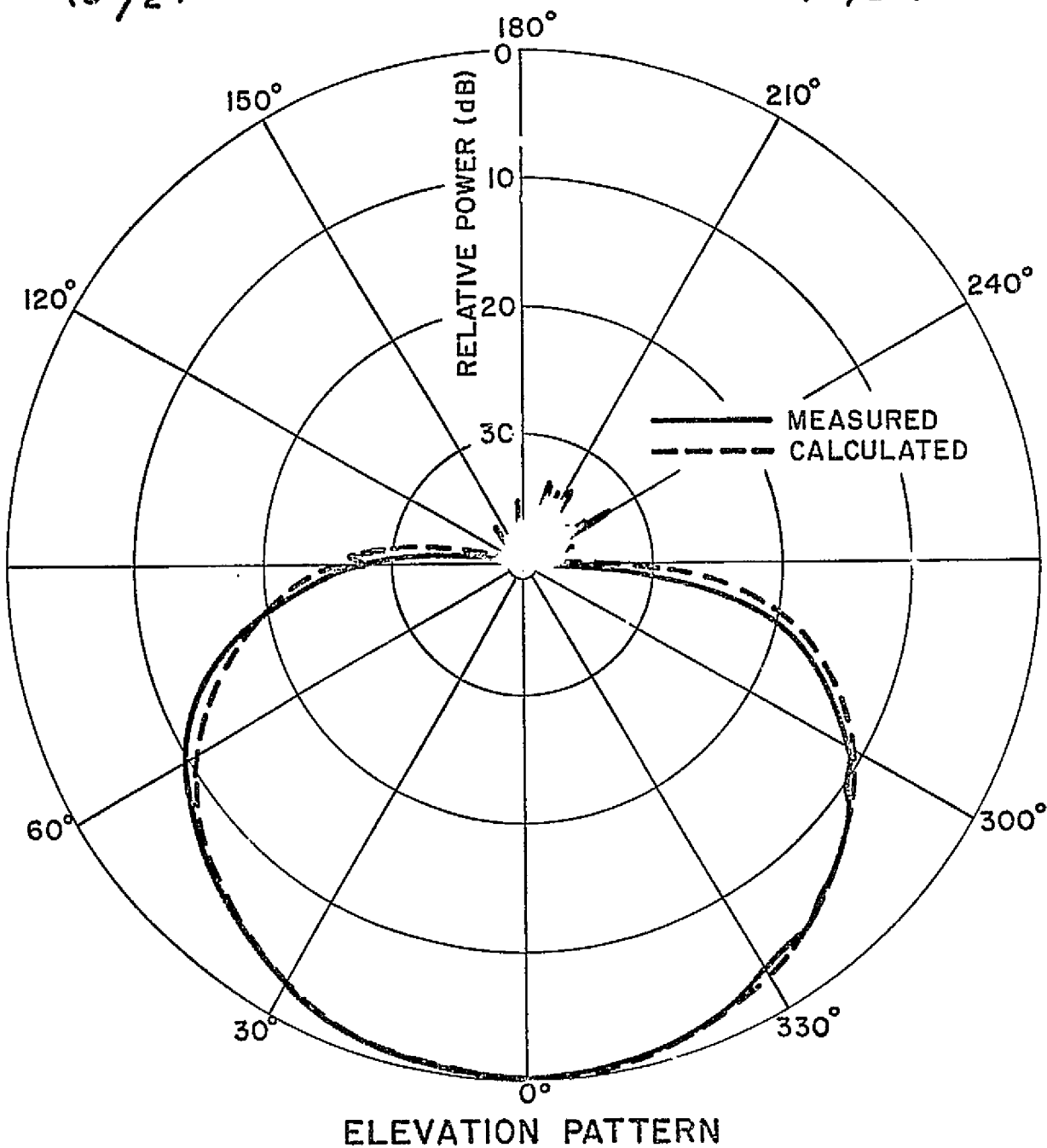WAVEGUIDE
(8 1/2")

SPACE SHUTTLE
WITH   RADOME
(6 1/2")

ELEVATION PATTERN

Fig. 12. Elevation pattern of axial slot on a 1/35th
scale model of space shuttle (with radome
included).

21

Fig. 13 shows the radiation pattern of the space shuttle with radome size being 2" and antennas mounted 1/2" away from radome. Note that the waveguide used here is the same KA-band waveguide used previously. The experimental results, which were taken at NASA, Langley Center, are also presented. The agreement between calculated and measured results show the applicability of theoretical predictions.

A further application of our solutions to the Boeing 737 aircraft also revealed good agreement between theoretical results and NASA scale model measurements as shown in Fig. 14. The 737 aircraft is modelled by a composite ellipse with a 1200" by 64.46" right ellipse and a 233.52" by 64.46" left ellipse. The size of the radome on 737 aircraft is approximately 186.97" and the antennas are located 3 wavelengths away from the radome at the frequency 3.18 GHz. The experimental results shown in these figures were obtained using an 1/11th scale model and performed at NASA, Langley Center. Again, vertical polization seems to have better forward coverage than horizontal polarization.

The phase error results from the interaction between the fuselage structure and antennas. This is an indication of the degree of distortion or effect the fuselage structure has on the performance of the antenna. It is the phase of the radiated field when the phase center of the antenna system is taken as the phase reference center. It is defined by

error phase = actual phase - line of sight phase

line of sight phase = free space phase of antenna
                      without aircraft present.

Both the radiation pattern and error phase plot may be used to determine the polarization selection of the MLS system.

The success of above results illustrates the capability of GTD solutions in determining the elevation plane radiation patterns of on-aircraft antennas. Consequently, the solution is extended to determine the elevation patterns of various aircrafts such as Boeing 707, B-1, and F15A. The results are shown in Figs. 15 to 17. In addition, the error phase plots are, also, presented.

CONCLUSIONS

High frequency solutions for the elevation plane patterns of on-aircraft antennas are presented in this report. The antennas are mounted on the fuselage near the radome, in that the forward sector coverage for the Microwave Landing System (MLS) is most critical. The solutions for the patterns without the radome are first presented and verified by experimental results taken at NASA (Langley) on a 1/35 scale model of the space shuttle. With that solution satisfactory the radome is added by neglecting the low

relative dielectric constant radome. This approximation leads to a truncated elliptic cylinder approximation for the aircraft profile. The additional edges are analyzed using the GTD and applied to several practical problems. In this case, the solutions are verified by scale model measurements taken on the 1/35 scale model of the space shuttle and 1/11 scale model of the 737 aircraft. In addition, results are presented for the basic elements (monopole, axial slot, and circumferential slot) mounted on various aircraft. As a result of this data, it is apparent that one antenna using horizontal polarization is not adequate for the complete omni coverage desired using the locations considered in this report. In addition, it is questionable whether vertical polarization coverage will be adequate using one antenna. These questions must be examined in the future both in terms of coverage obtainable at several locations on various aircraft and in terms of the coverage necessary for such a system to function properly.

In order to answer the antenna coverage question, the theoretical solutions for the complete volumetric patterns must be developed. The roll plane program [5] previously developed is adquate for most of the volumetric pattern except near the nose or tail. This limitation is due to the infinite elliptic cylinder approximation of the fuselage. However, by modifying our elevation plane program, these sectors can be successfully handled. In addition, the cockpit can be taken into account using the flat plate model previously used to analyze the wings in the roll plane. Using this approach, the complete volumetric pattern can be obtained using one model consisting of a composite ellipse to which are attached flat plates. As a result of this simplified model, the program should be very efficient and require little storage.

As the solutions are developed, they will be applied to various practical examples and compared against scale model measurements. Two such studies which are proposed involve the T-39 being studied by Bendix and the 737 system studied at NASA (Langley). In both cases, numerical solutions shall provide pattern performance information.

23

HORIZONTAL POL.
WAVEGUIDE
(2 ½")

SPACE SHUTTLE
WITH RADOME
(2")
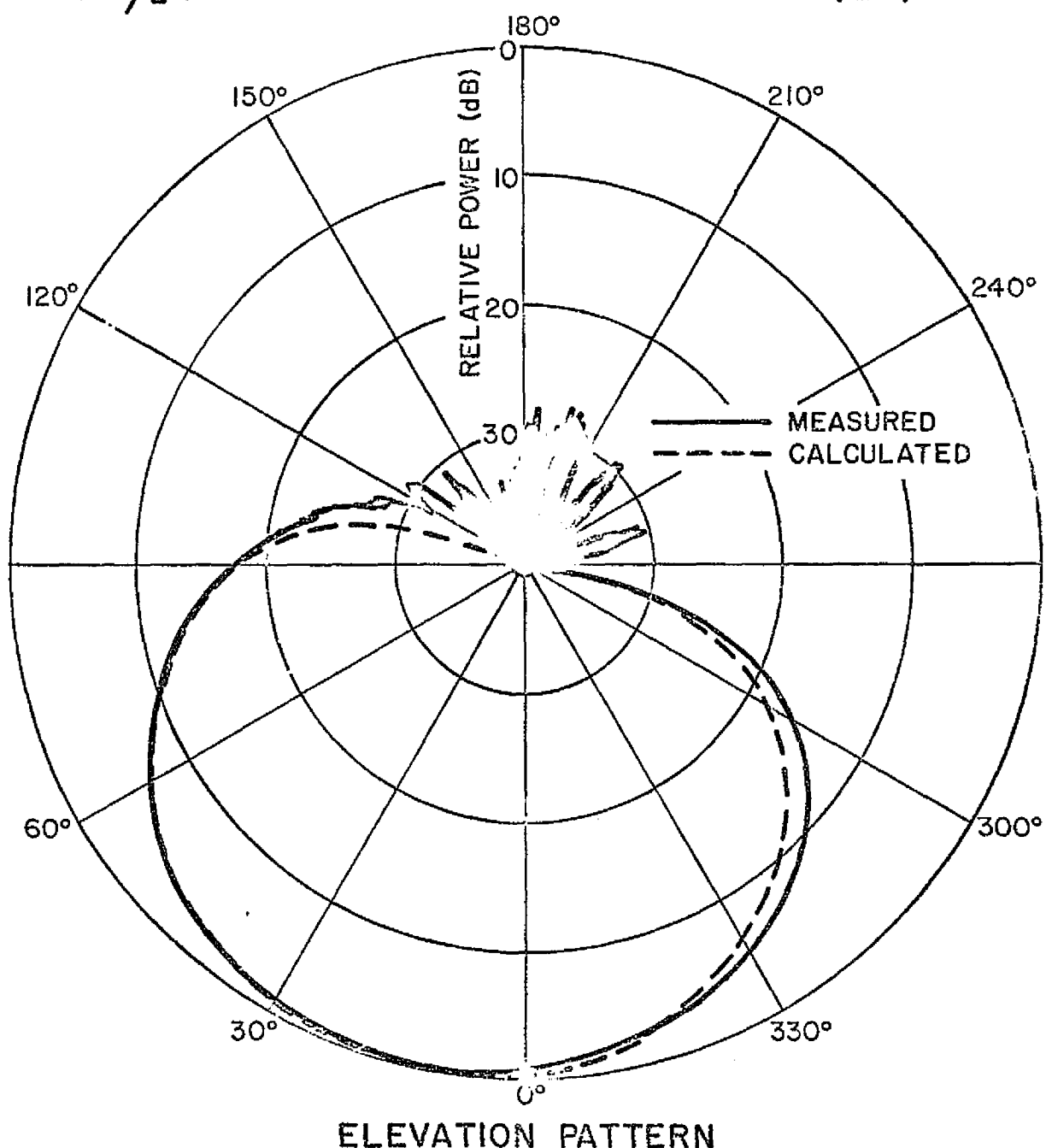
ELEVATION PATTERN

Fig. 13. Elevation pattern of axial slot on a 1/35th
scale model of space shuttle (with radome
being 2").

24
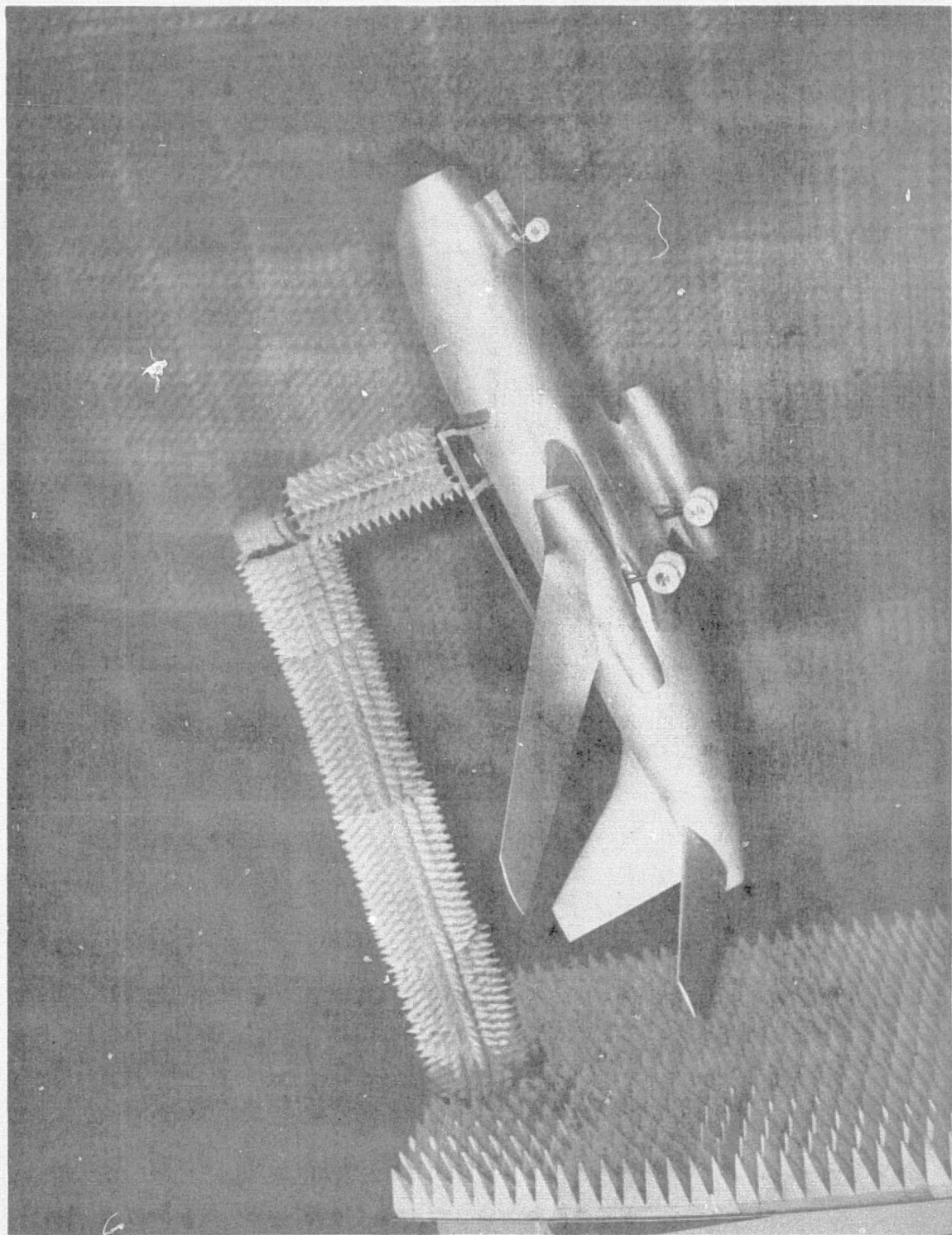
Fig. 14a. The scale model (1/11) of Boeing 737 aircraft
in Anechoic Chamber at NASA, Langley Center.

VERTICAL POL.
MONOPOLE

737 AIRCRAFT
WITHOUT LANDING GEAR
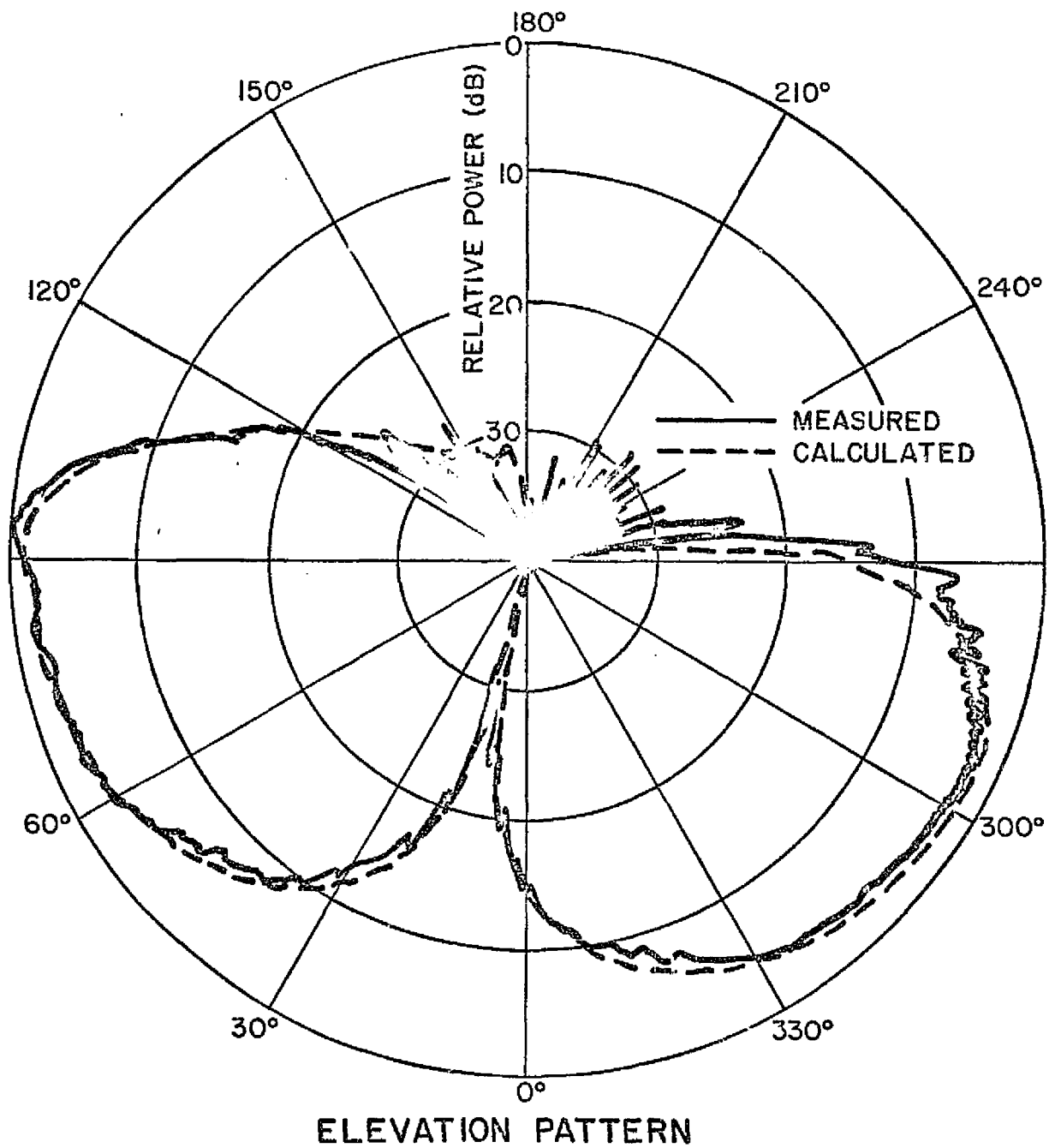
ELEVATION PATTERN

Fig. 14b. Elevation pattern of monopole on a 1/11th
scale model of Boeing 737 aircraft.

26

ERROR PHASE IN DEGREES

-45   -30   -15   0   15   30   45
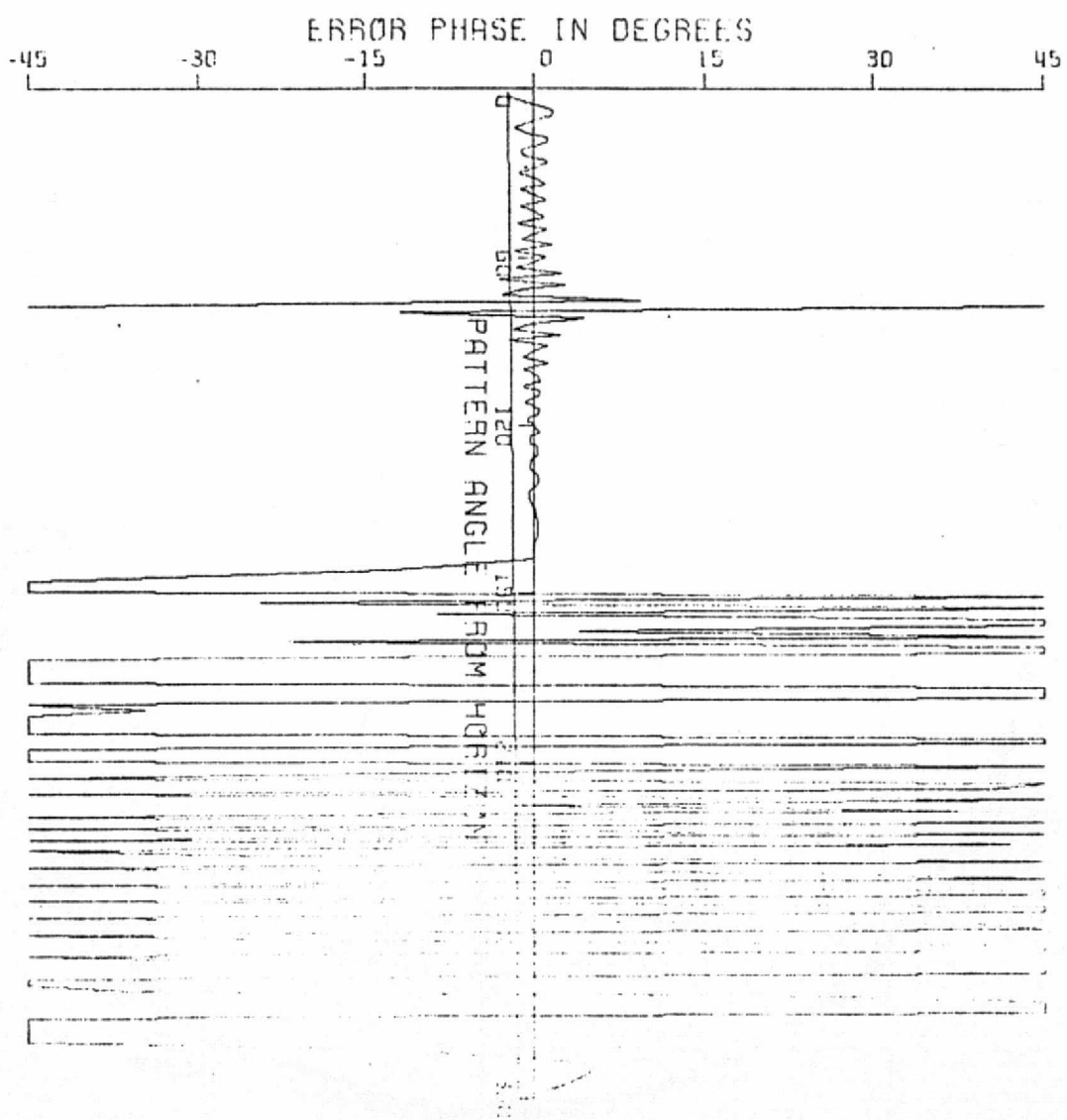
Fig. 14c.   Phase error plot of monopole on a 1/11th
            scale model of Boeing 737 aircraft.

27

VERTICAL POL.
WAVEGUIDE

737 AIRCRAFT
WITHOUT LANDING GEAR
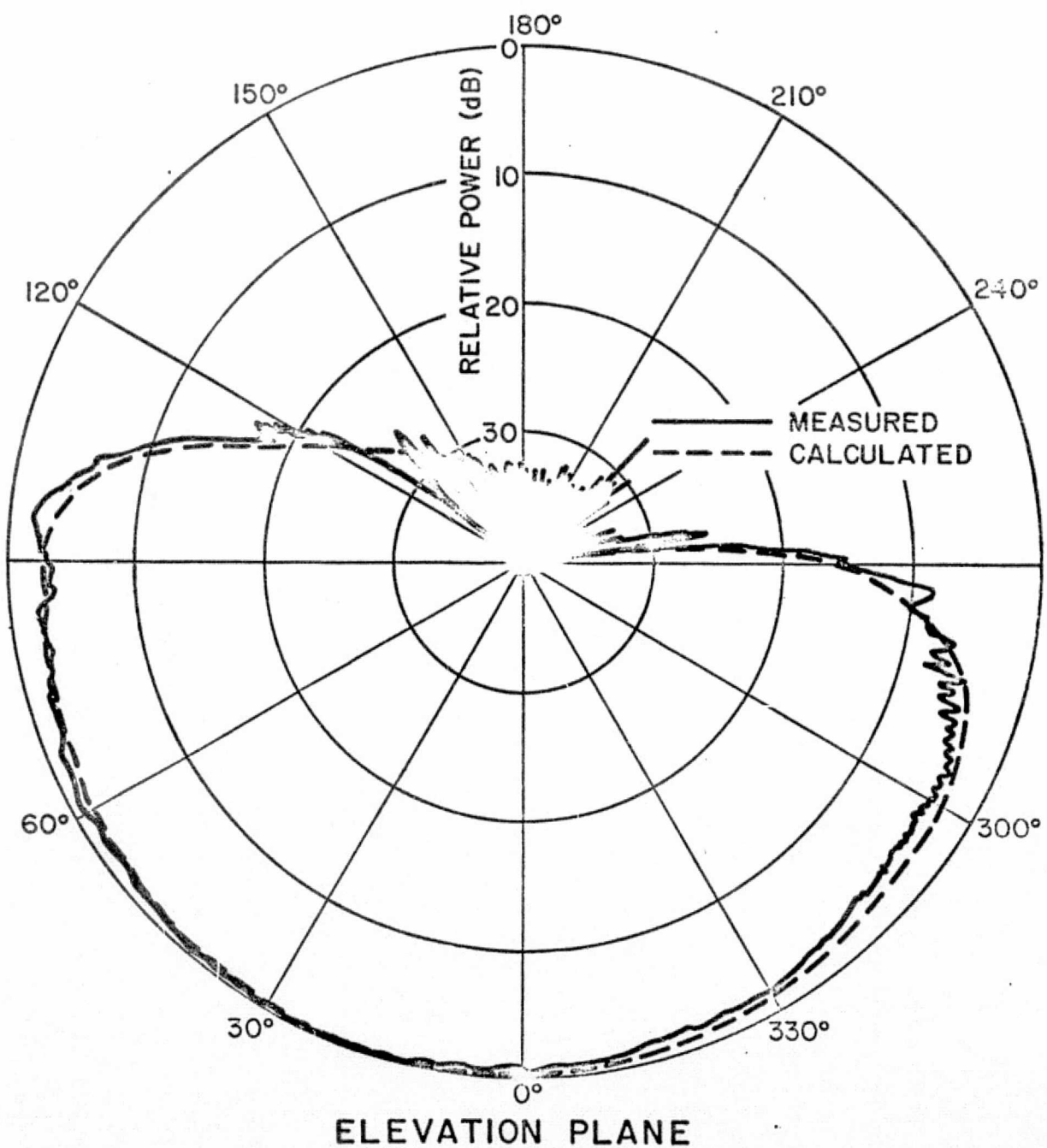
Fig. 14d. Elevation pattern of circumferential slot
on a 1/11th scale model of Boeing 737
aircraft.

28
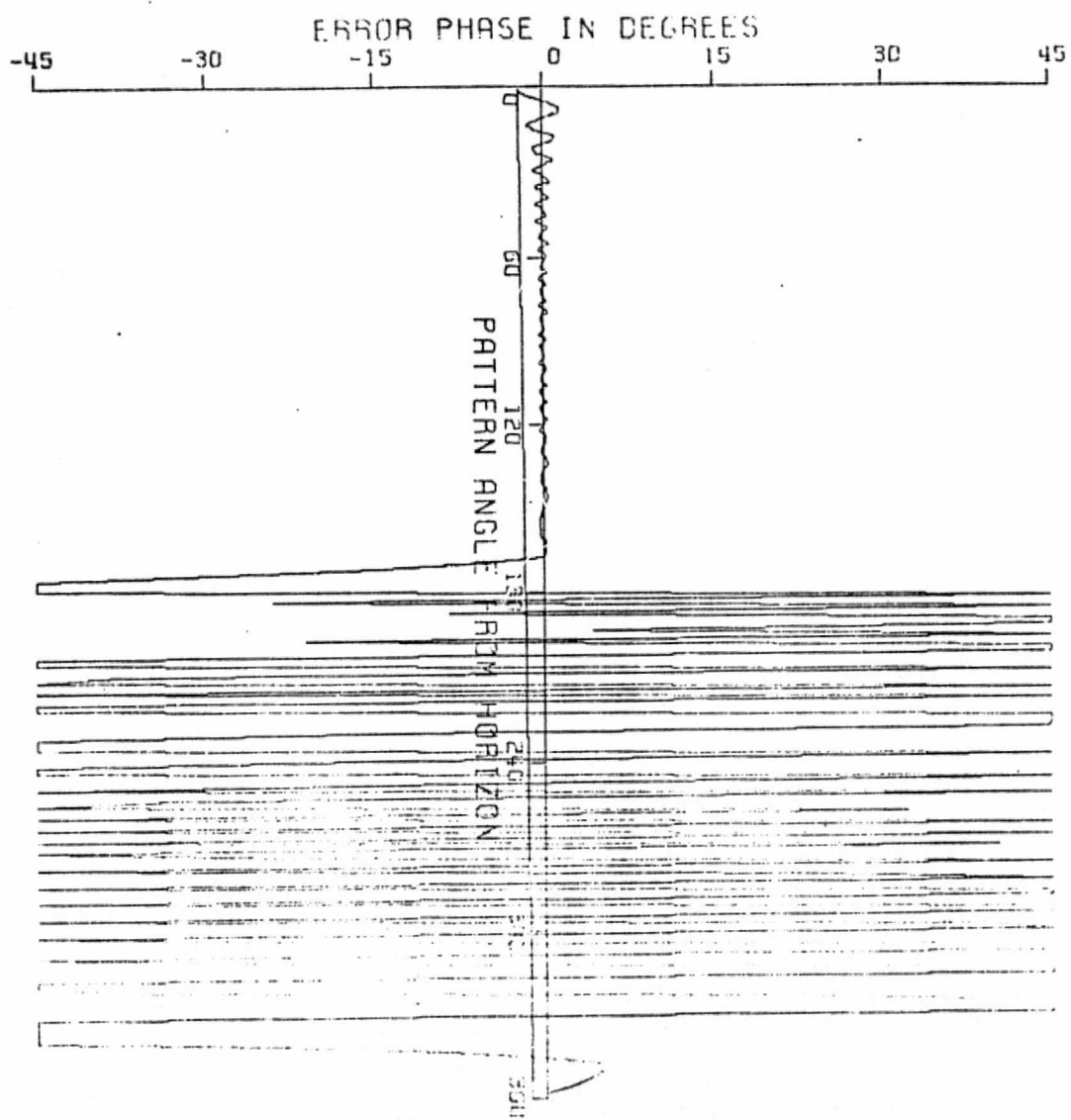
Fig. 14e. Phase error plot of circumferential slot
on a 1/11th scale model of Boeing 737
aircraft.

29

HORIZONTAL POL.
WAVEGUIDE

737 AIRCRAFT
WITHOUT LANDING GEAR
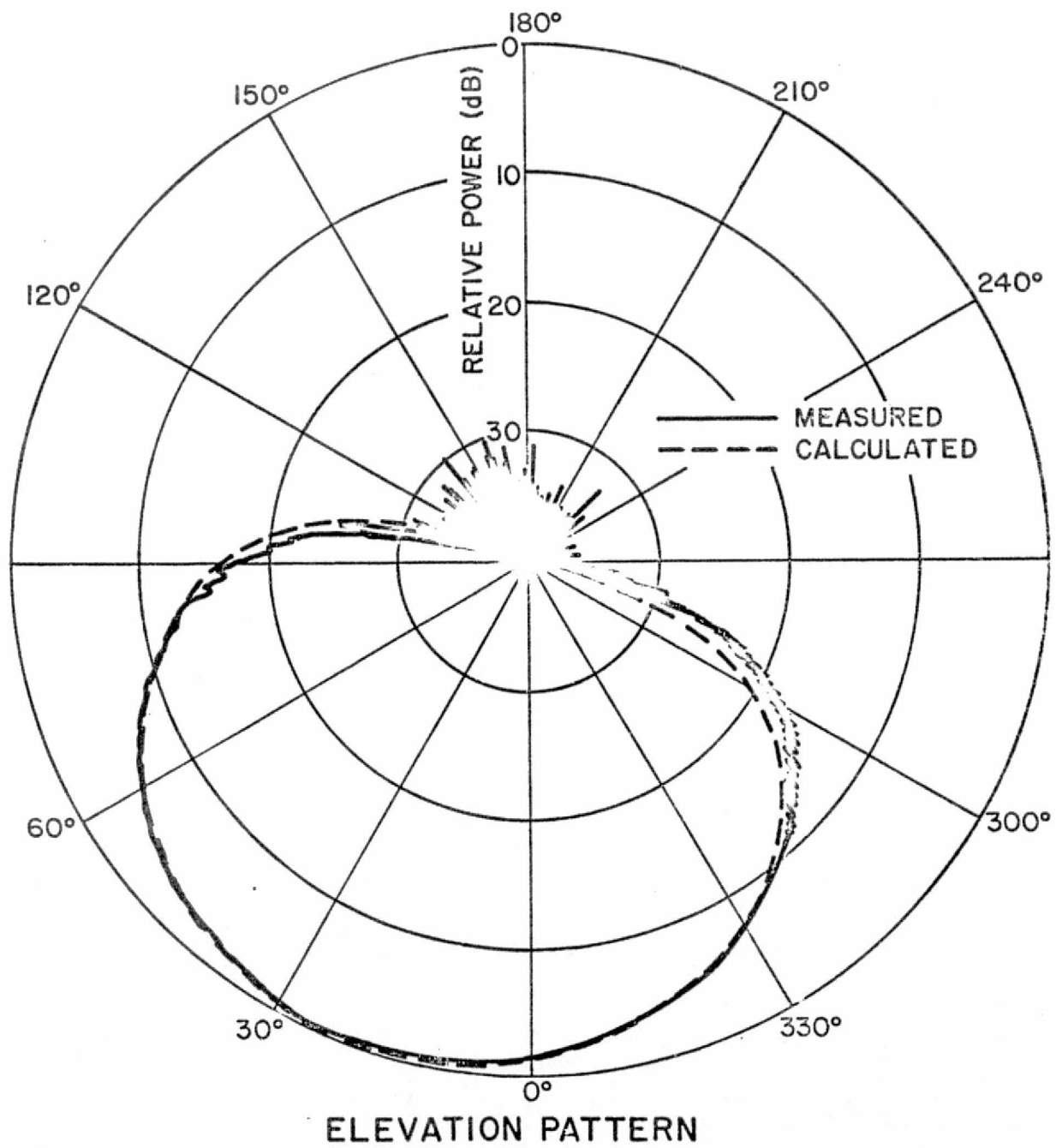
ELEVATION PATTERN

Fig. 14f. Elevation pattern of axial slot on a 1/11th scale model of Boeing 737 aircraft.

30

ERROR PHASE IN DEGREES
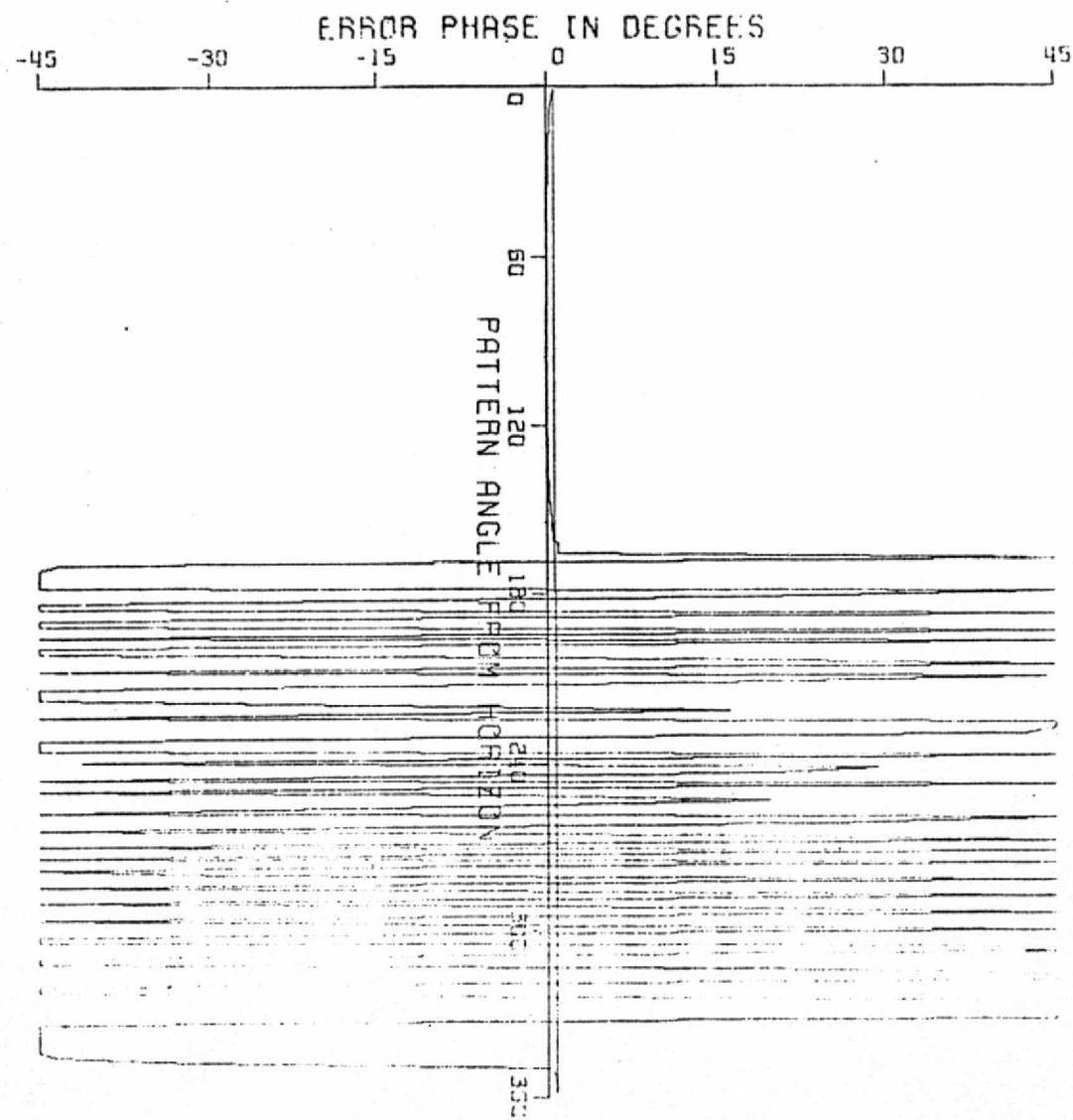
Fig. 14g. Phase error plot of axial slot on a 1/11th
scale model of Boeing 737 aircraft.

31
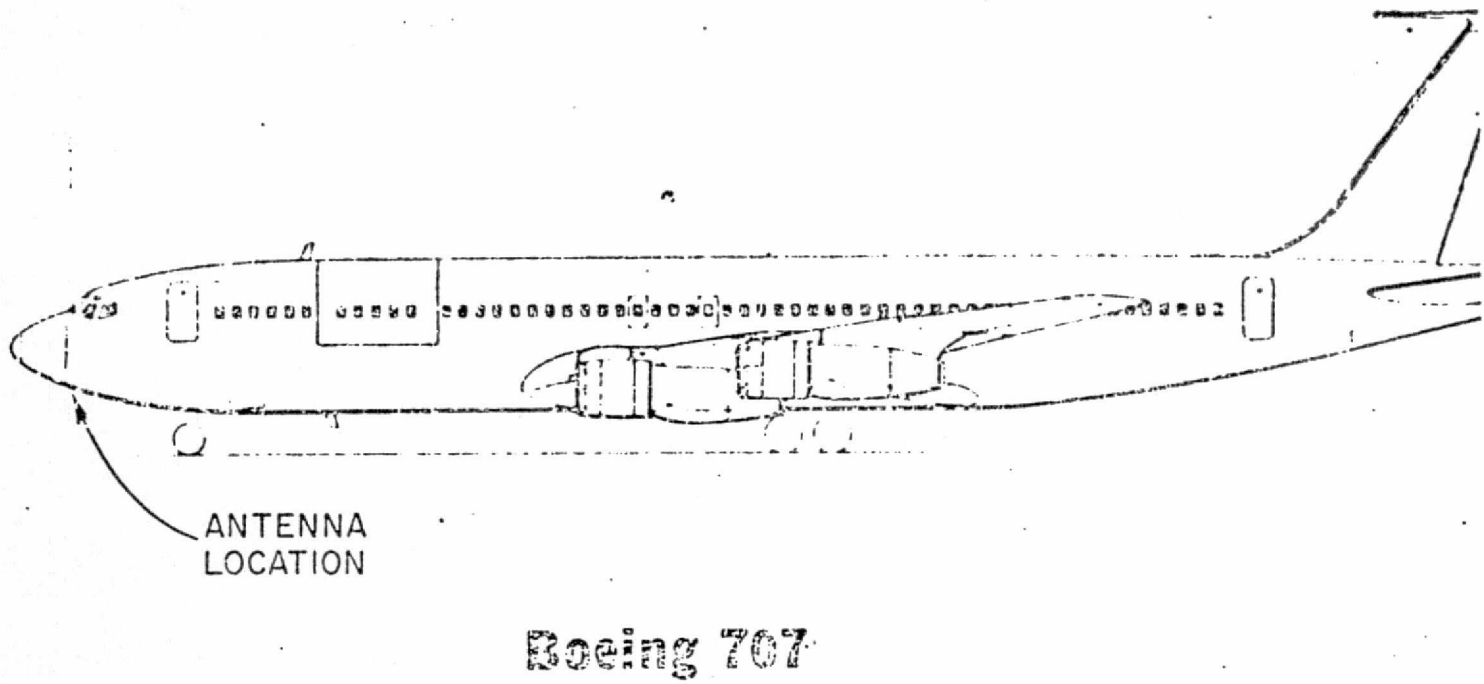
ANTENNA
LOCATION

Boeing 707

Fig. 15a. The profile of Boeing 707 aircraft and the position of
antenna location being considered (3 wavelengths from
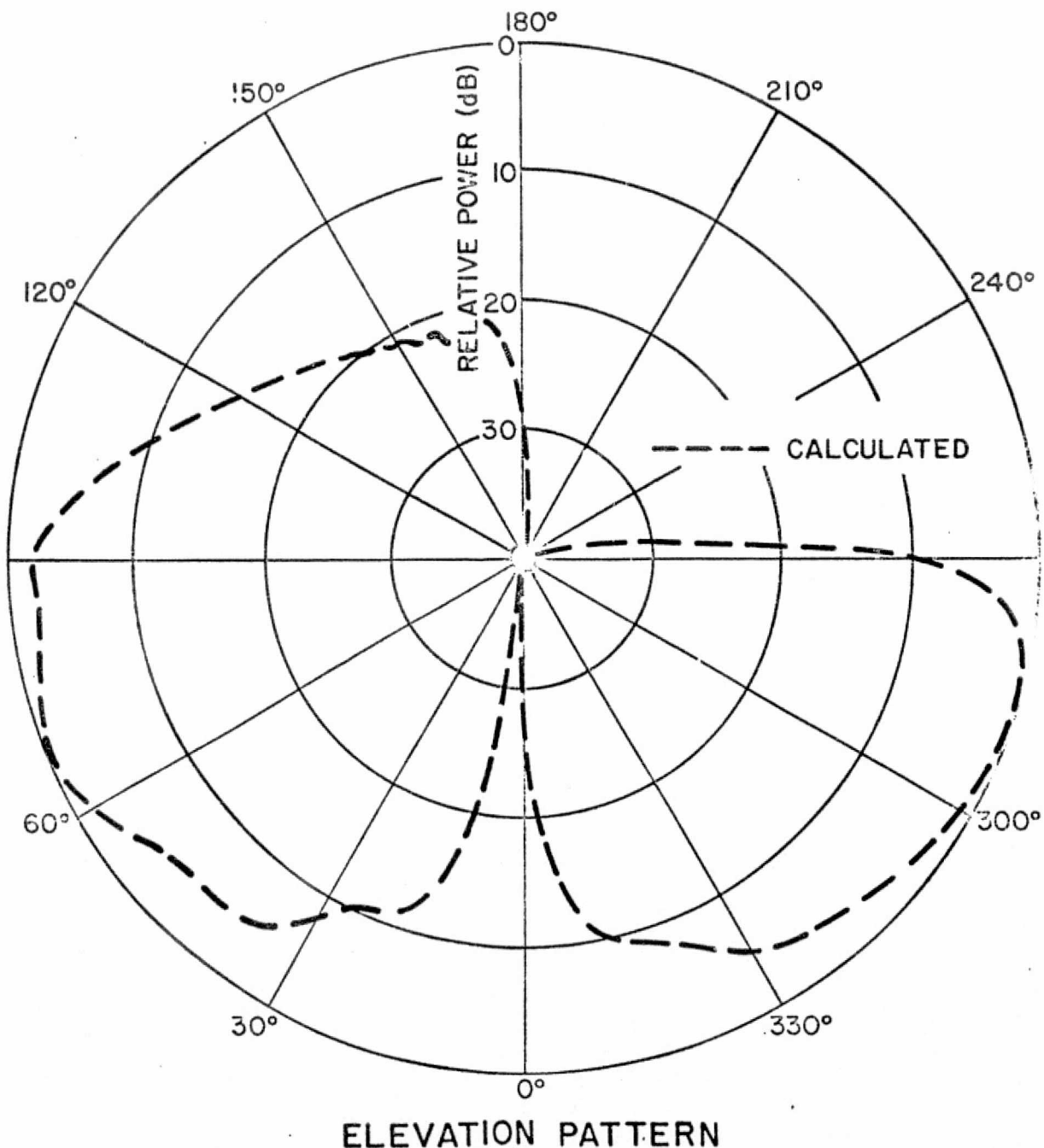the radome).

VERTICAL POL.
MONOPOLE

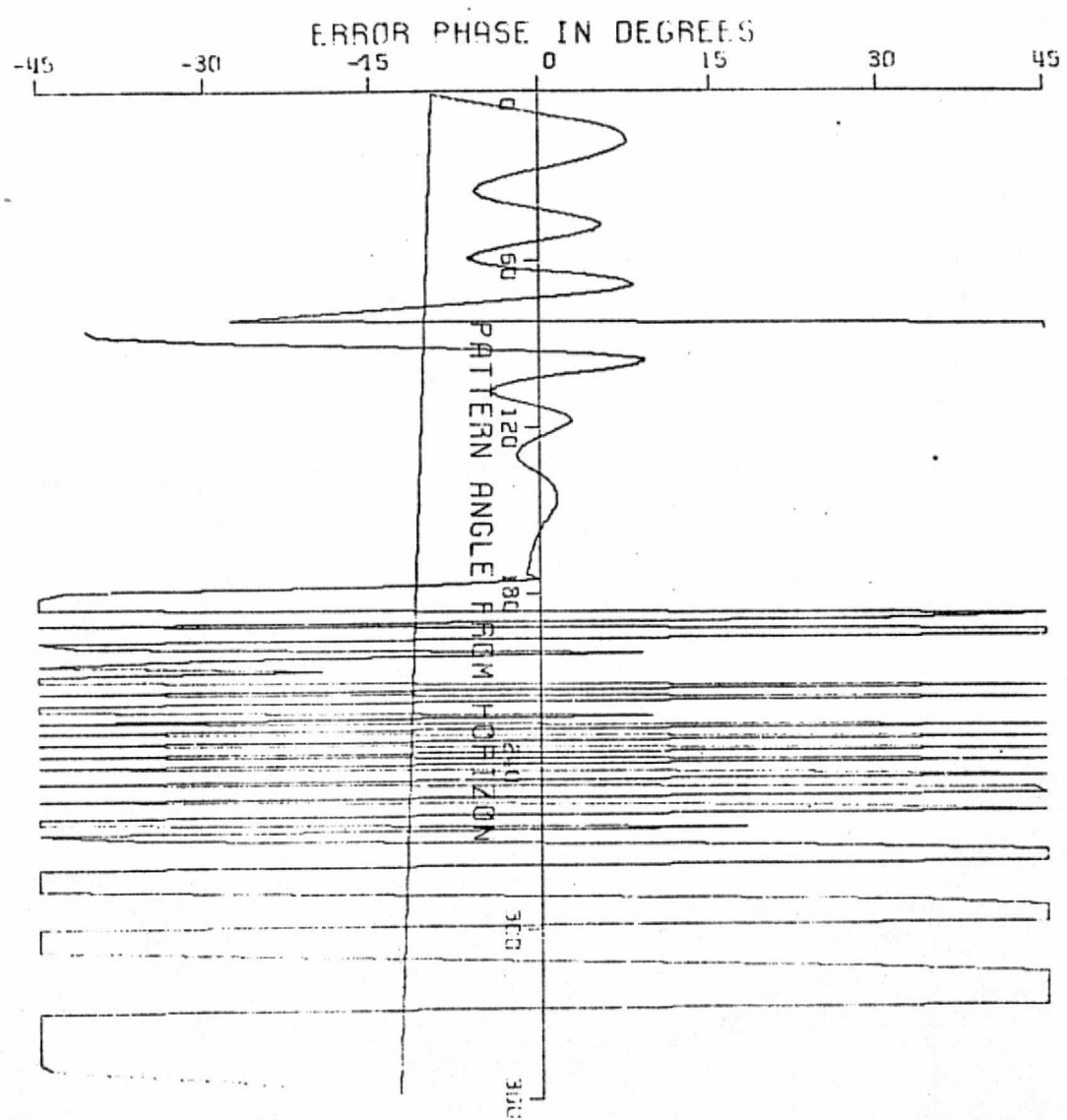# 707 AIRCRAFT
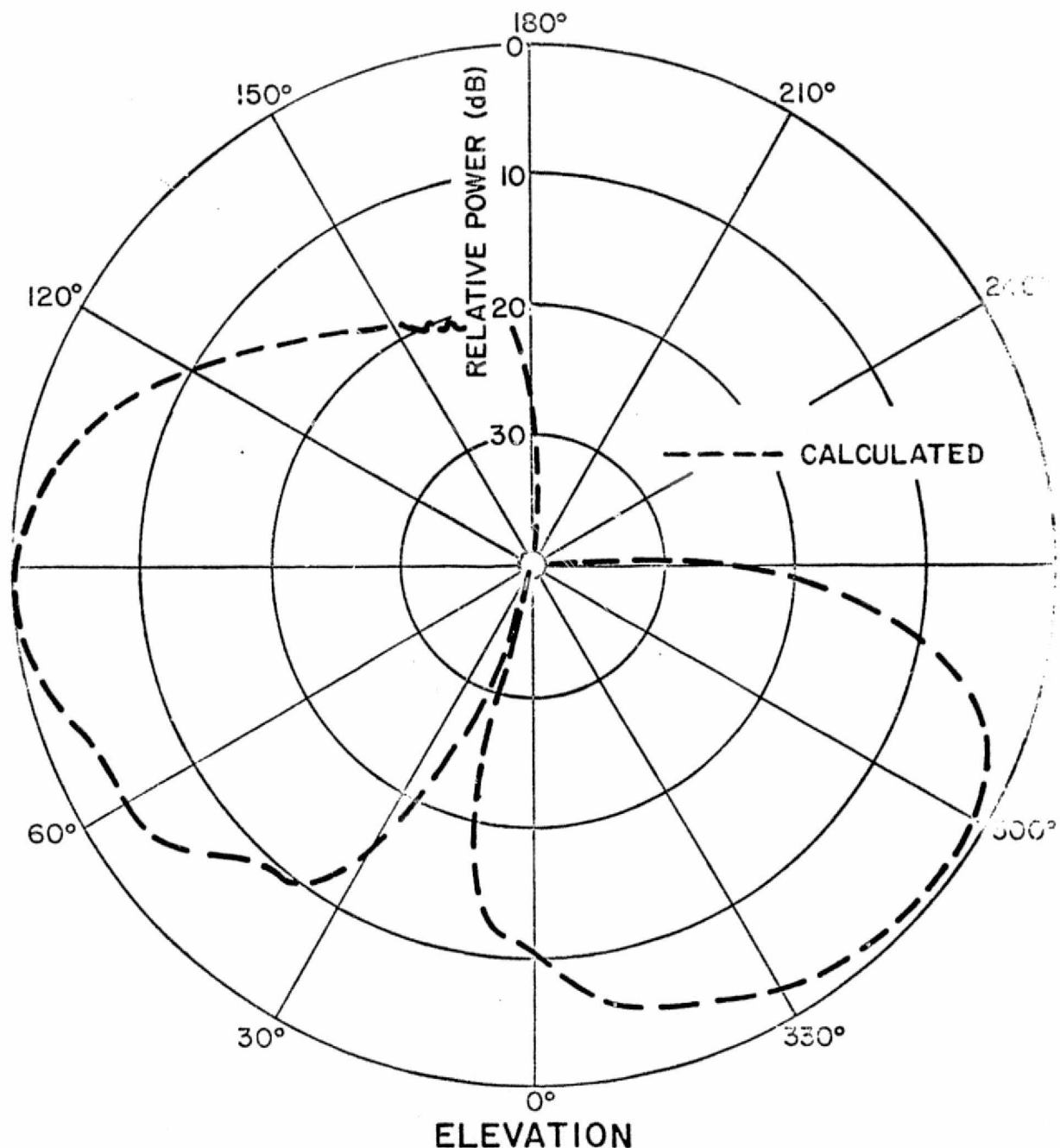
Fig. 15b. Elevation pattern of monopole on a Boeing
707 aircraft.

33
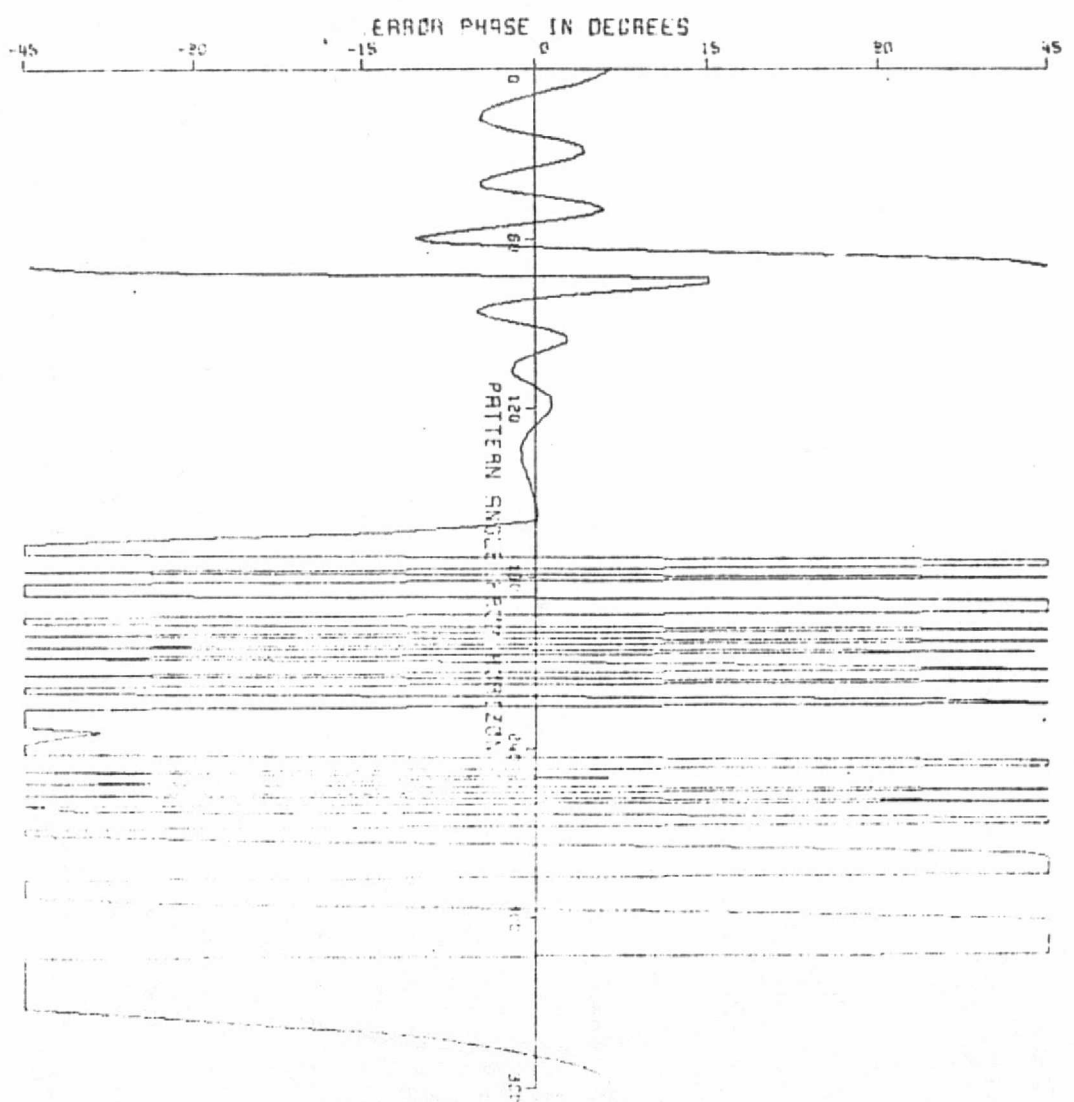
Fig. 15c. Phase error plot of monopole on a Boeing
707 aircraft.
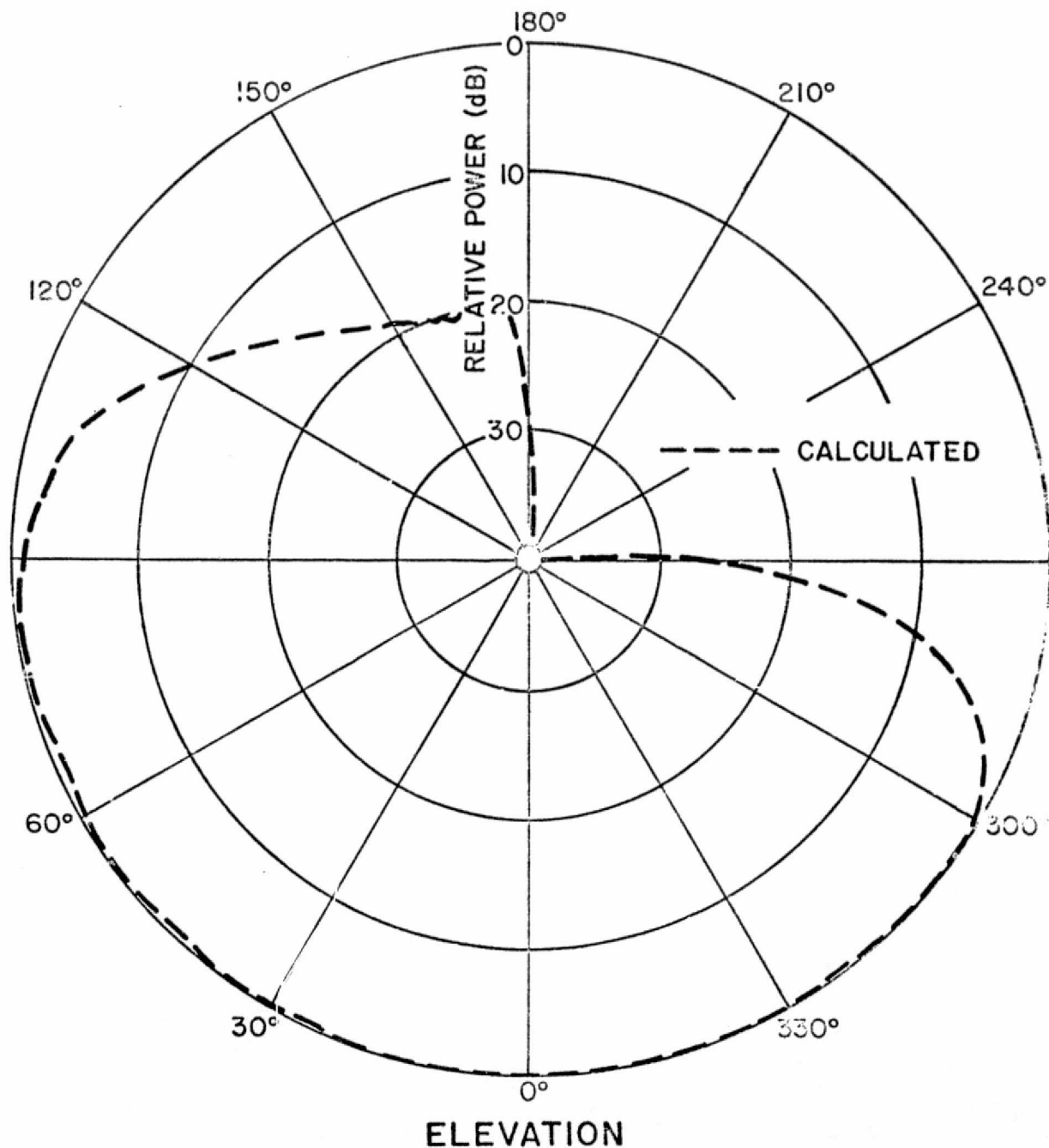
34

Fig. 15d. Elevation pattern of circumferential slot on a Boeing 707 aircraft.

35

ERROR PHASE IN DEGREES
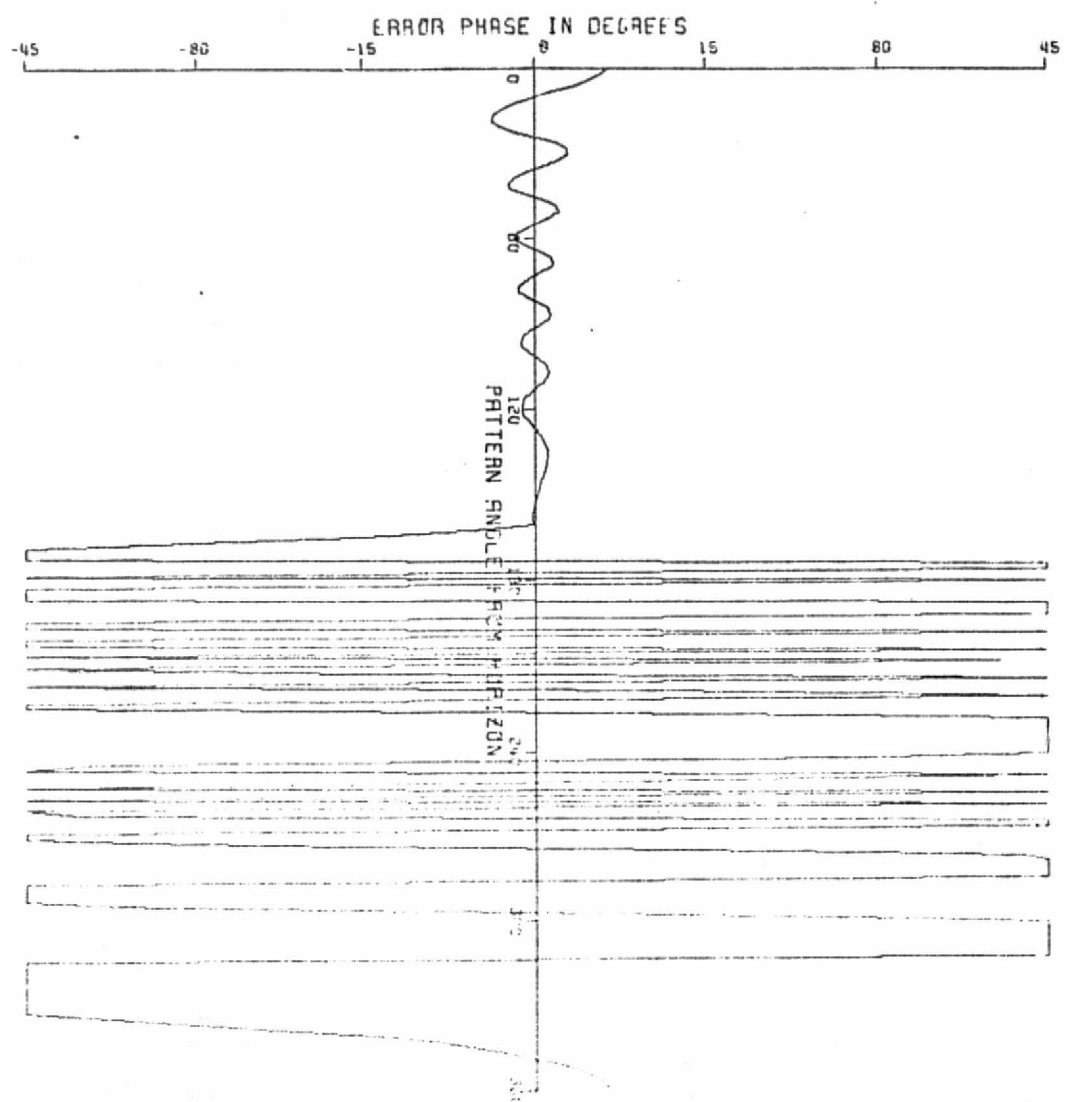
Fig. 15e.   Phase error plot of circumferential slot
on a Boeing 707 aircraft.

36
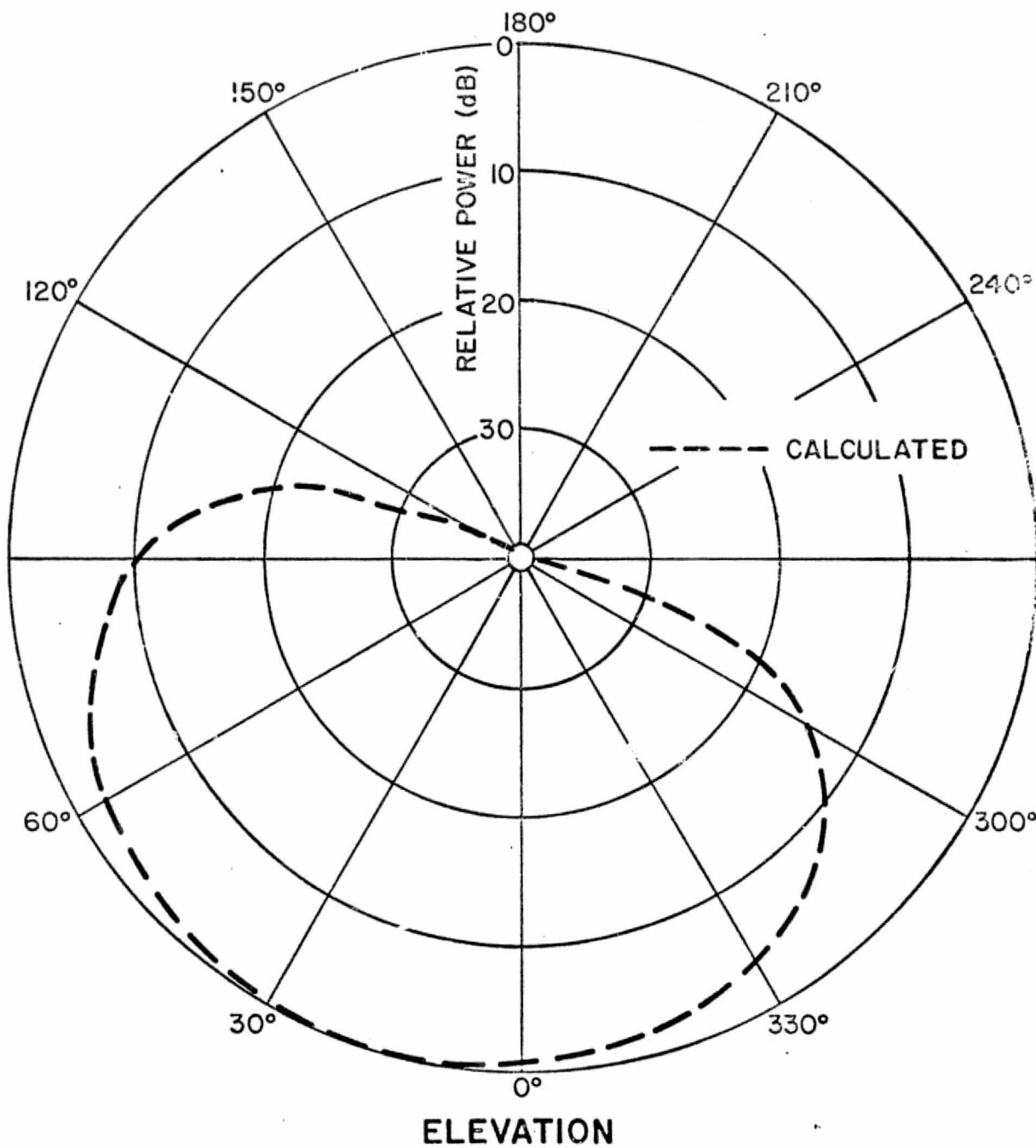
Fig. 15f. Elevation pattern of axial slot on a Boeing
707 aircraft.
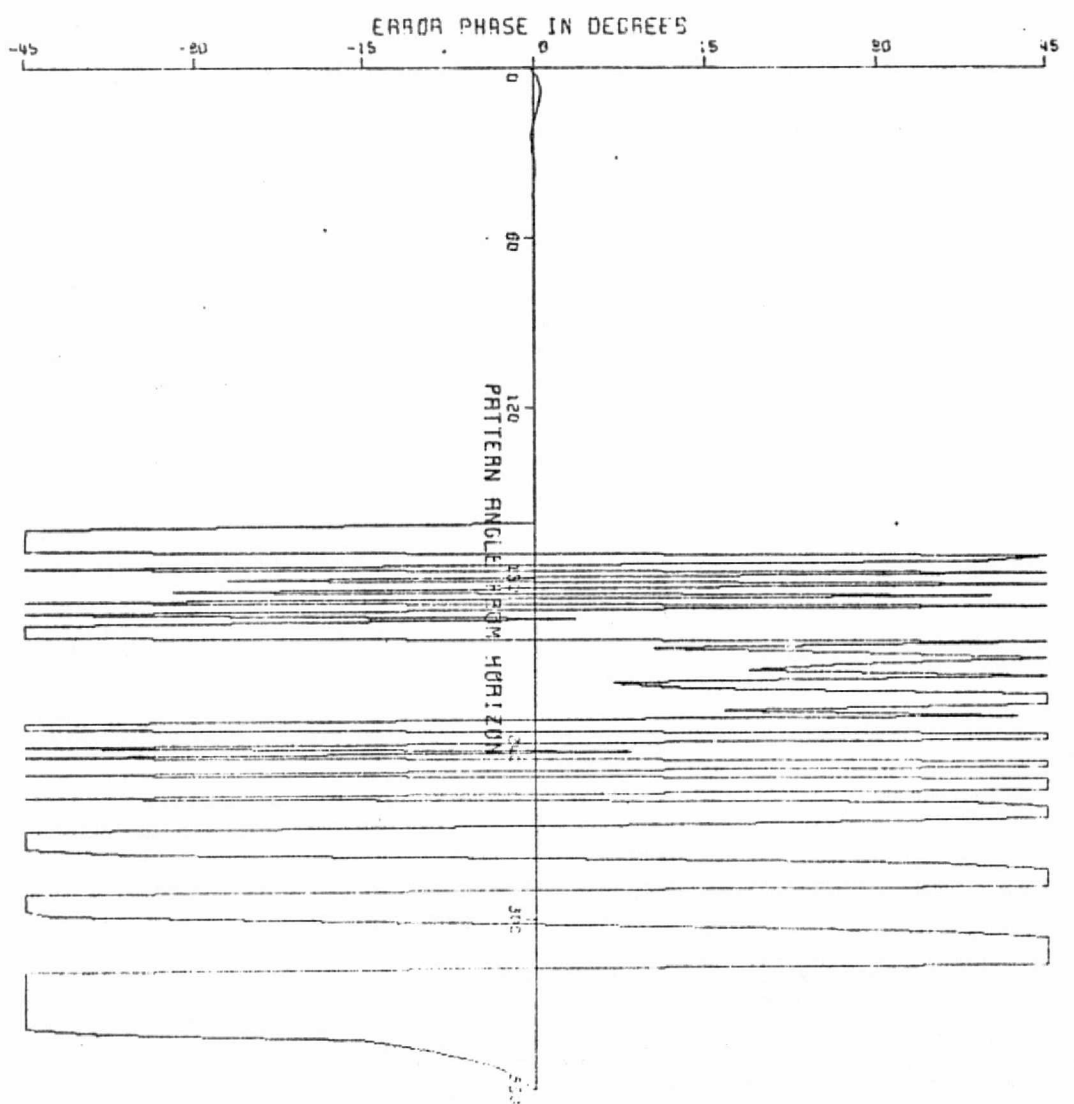
Fig. 15g. Phase error plot of axial slot of a
Boeing 707 aircraft.

38

ANTENNA
LOCATION

B-1
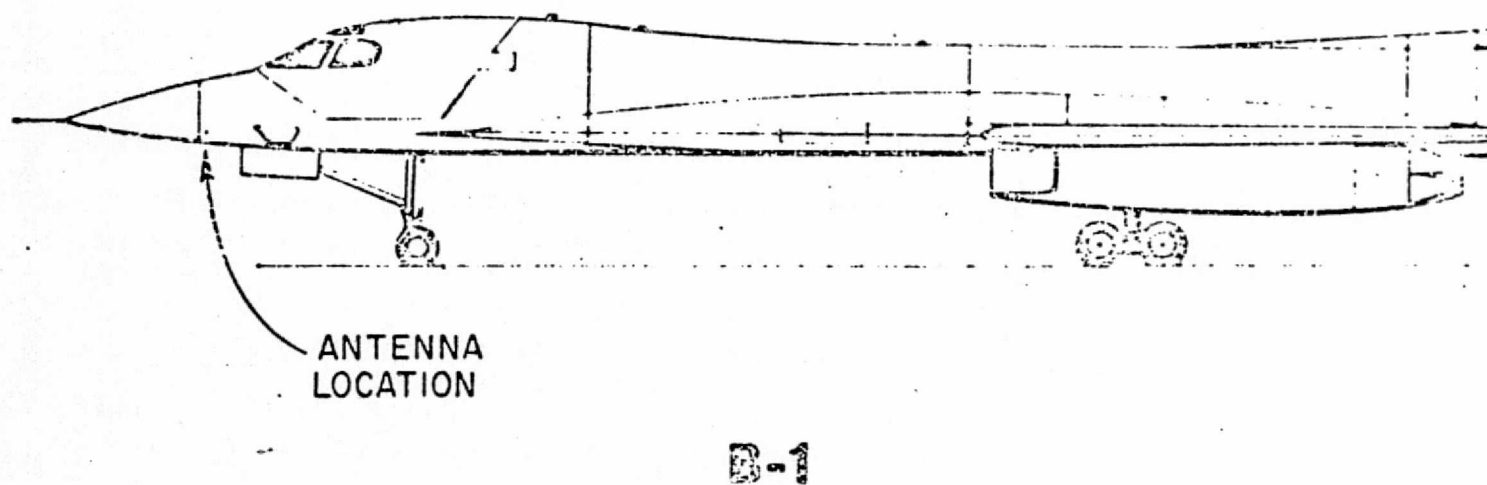
Fig. 16a. The profile of B-1 aircraft and the position of antenna
location being considered (3 wavelengths from the radome).

VERTICAL POL.
MONOPOLE

B—I AIRCRAFT

ELEVATION PATTERN

Fig. 16b. Elevation pattern of monopole on a B-1 aircraft.

ERROR PHASE IN DEGREES

Fig. 16c.   Phase error plot of monopole on a B-1
            aircraft.

41

VERTICAL POL.
SLOT

B—I AIRCRAFT
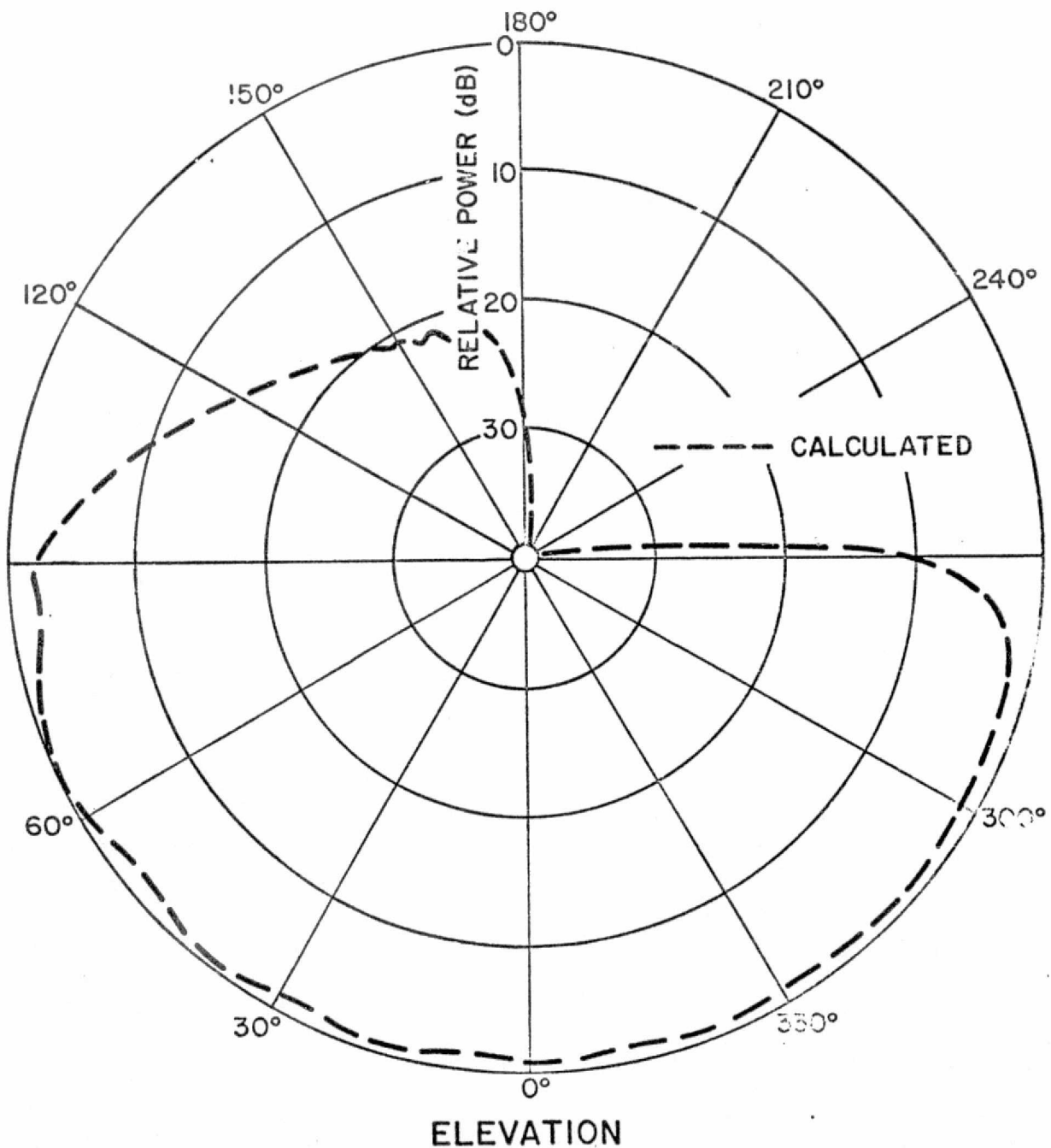
Fig. 16d. Elevation pattern of circumferential slot
on a B-1 aircraft.

42
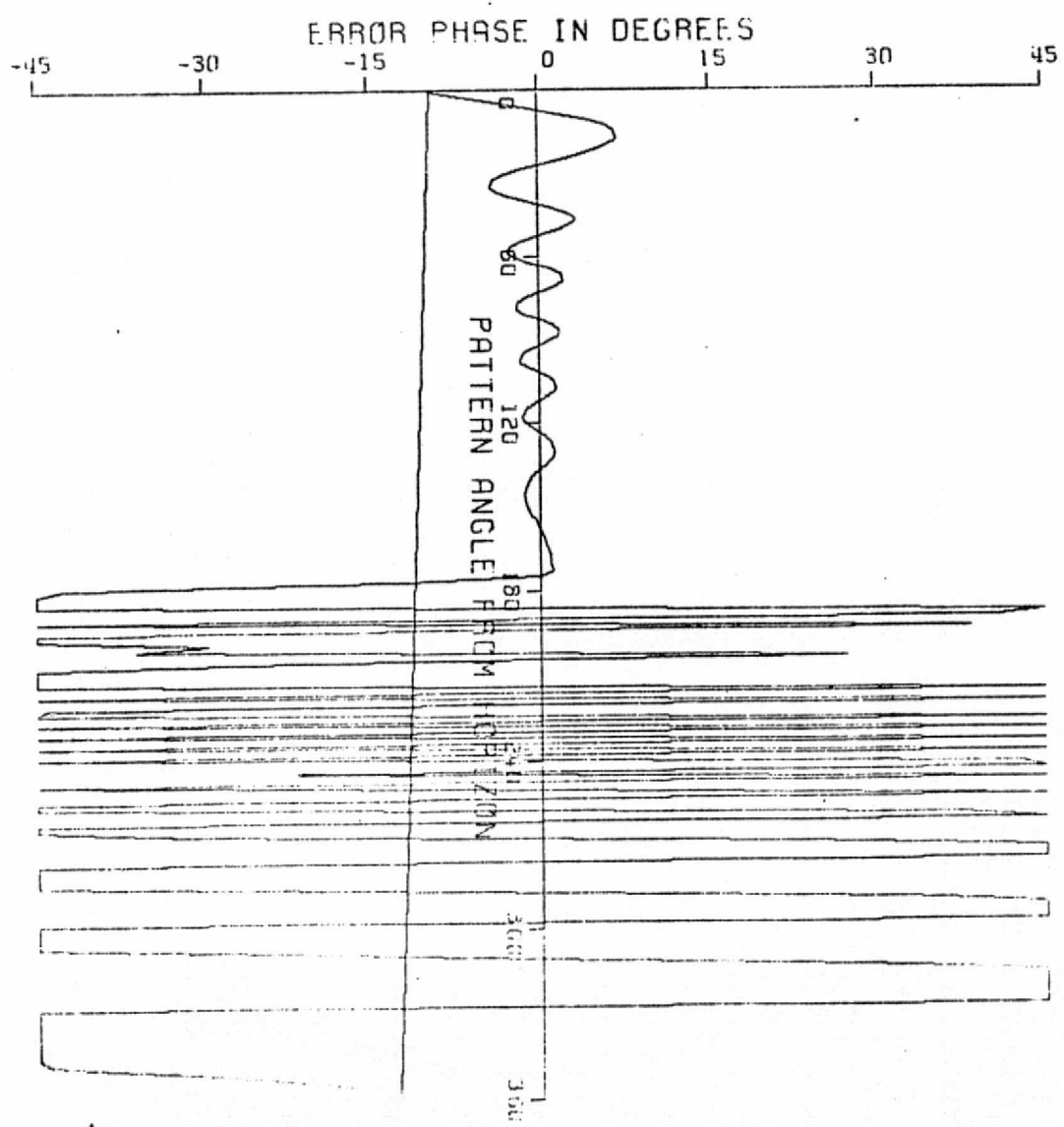
Fig. 16e.   Phase error plot of circumferential slot
on a B-1 aircraft.

43

HORIZONTAL POL.
SLOT

B—I AIRCRAFT
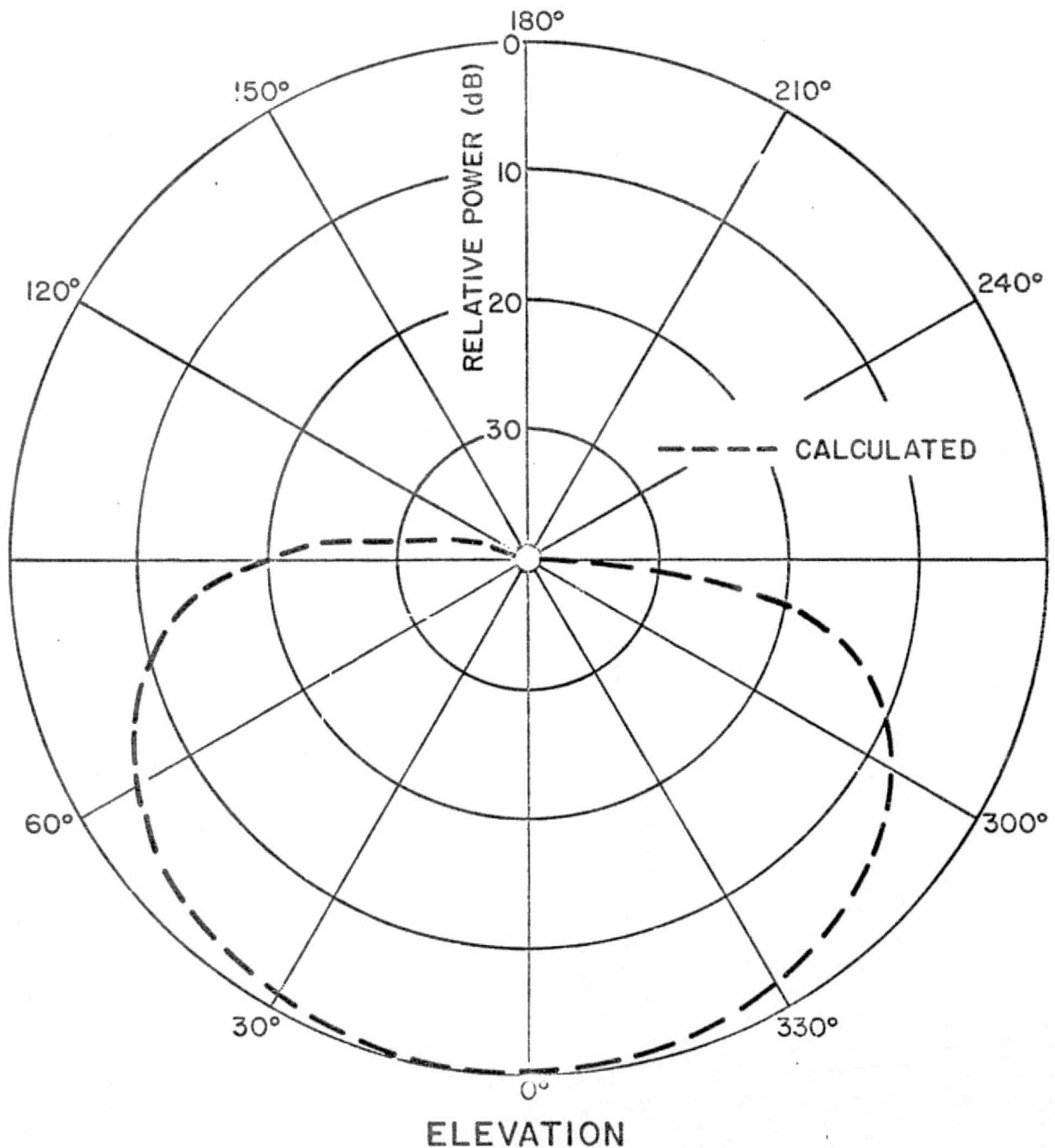
Fig. 16f.   Elevation pattern of axial slot of
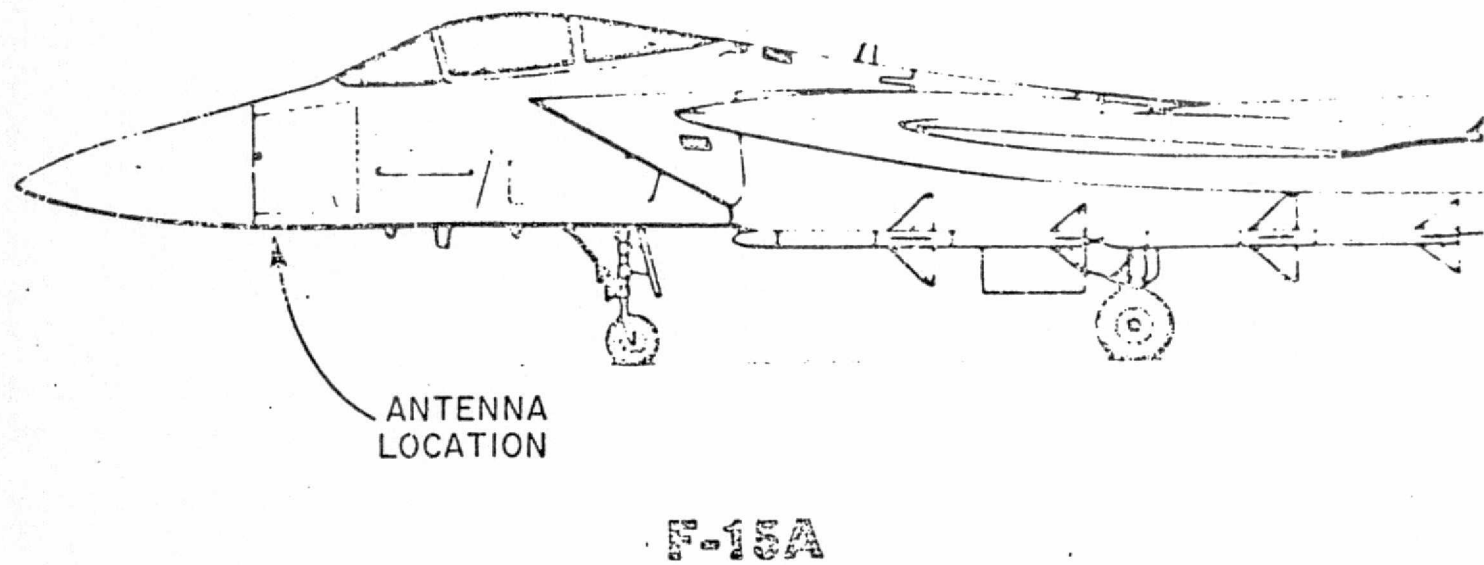B-1 aircraft.

ERROR PHASE IN DEGREES
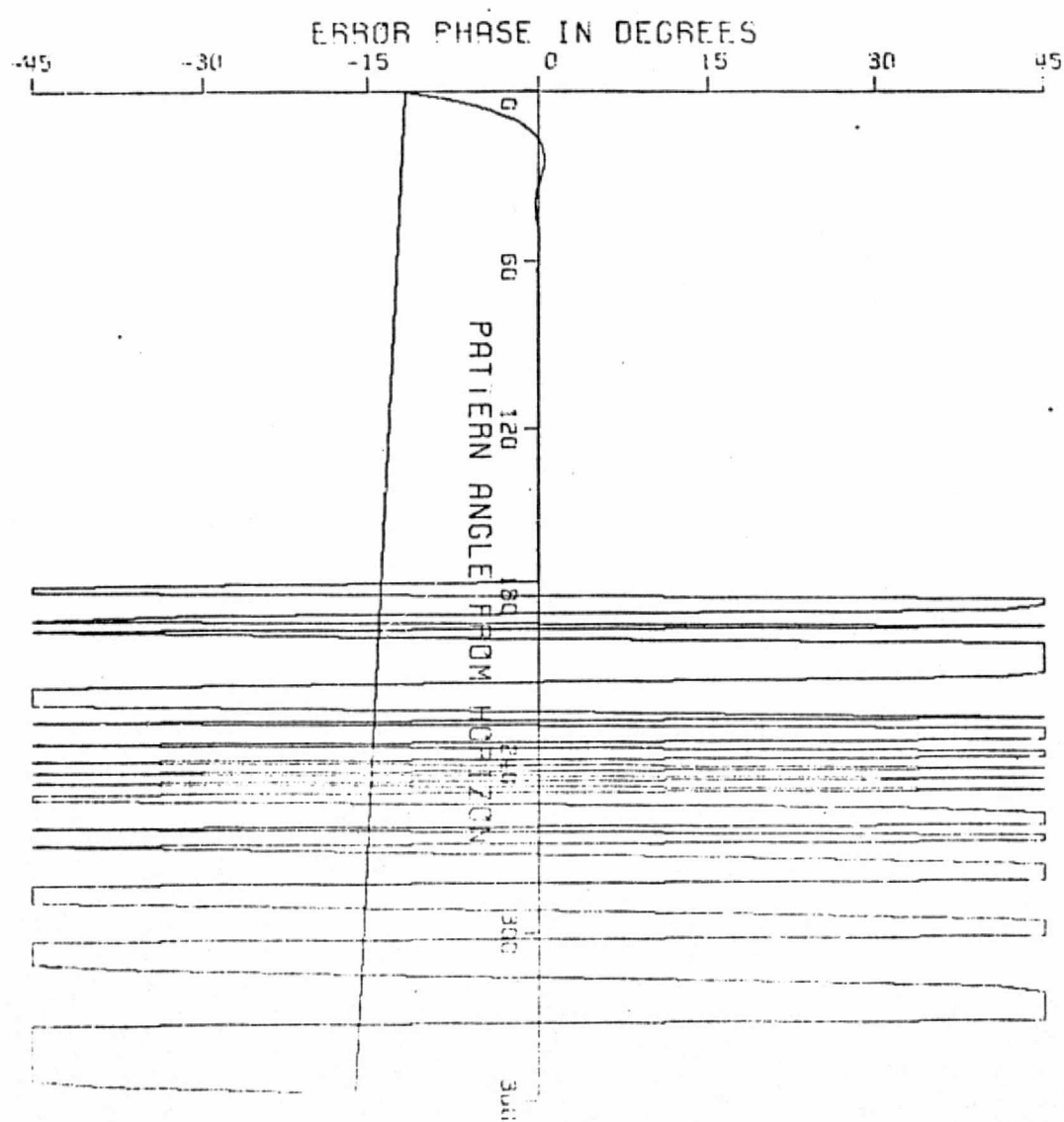
Fig. 16g. Phase error plot of axial slot of
           B-1 aircraft.

ANTENNA
LOCATION

F-15A

Fig. 17a. The profile of F-15 aircraft and the position of antenna
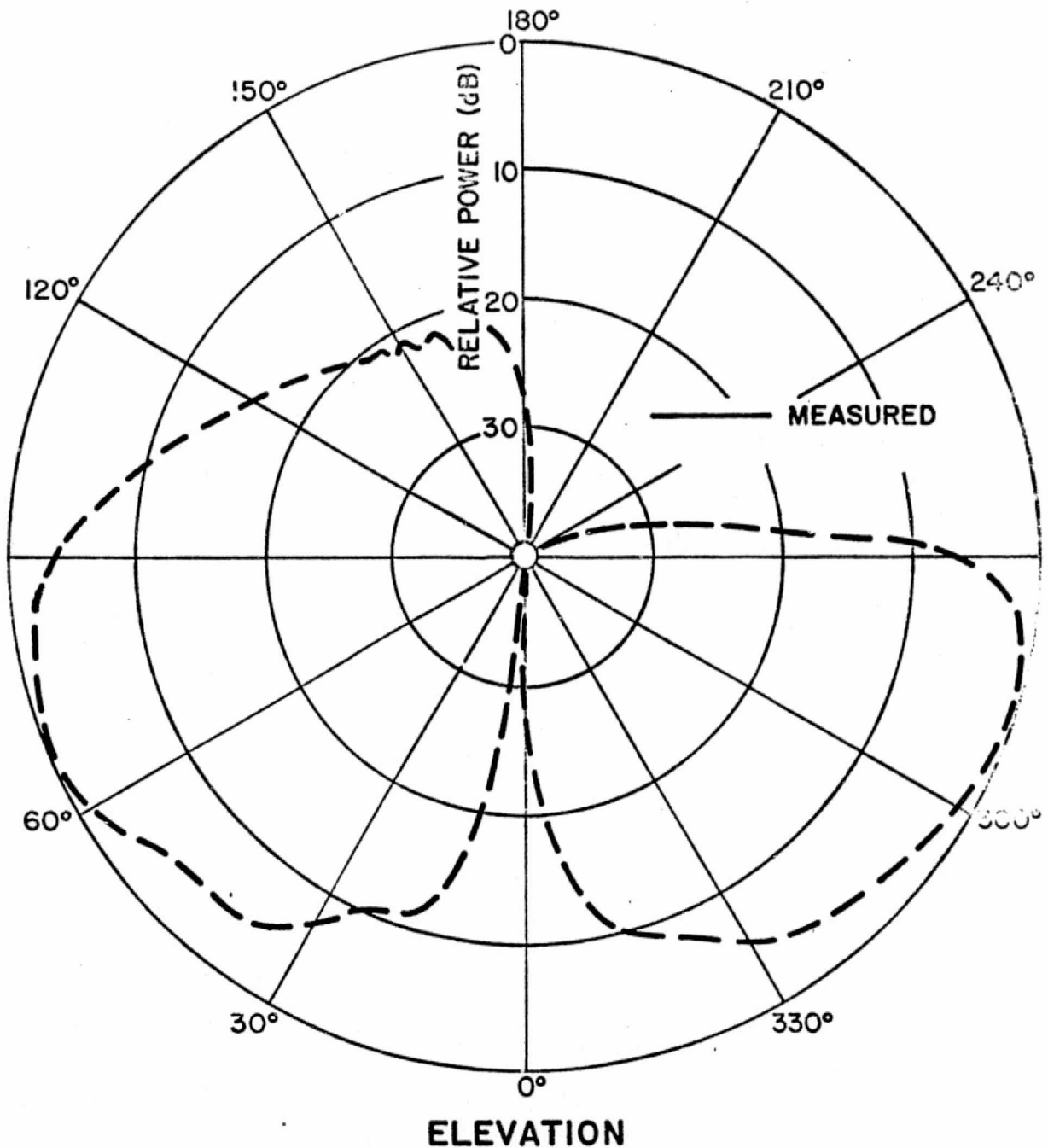location being considered (3 wavelengths from the radome).
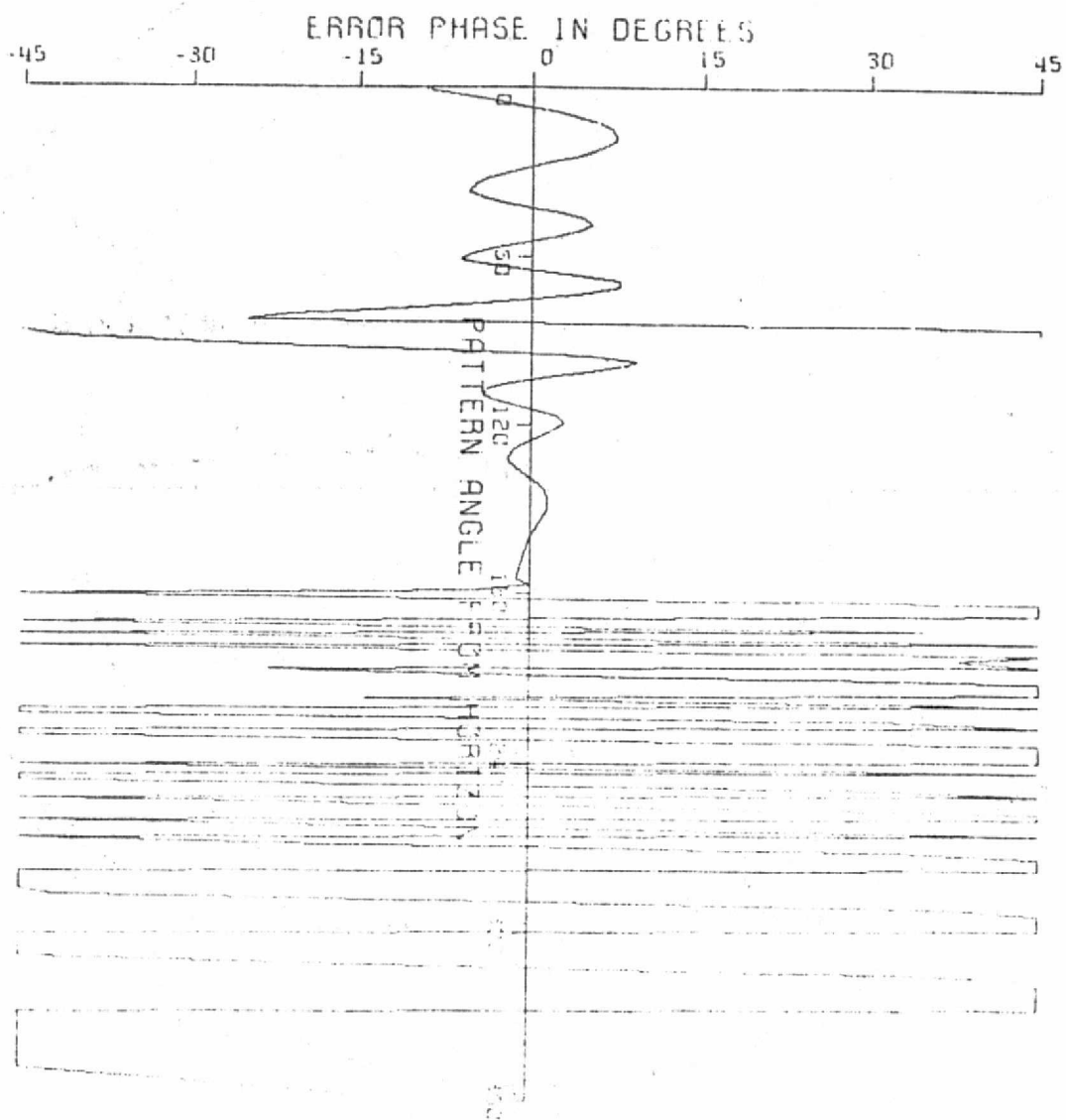
Fig. 17b. Elevation pattern of monopole on B-15 aircraft.

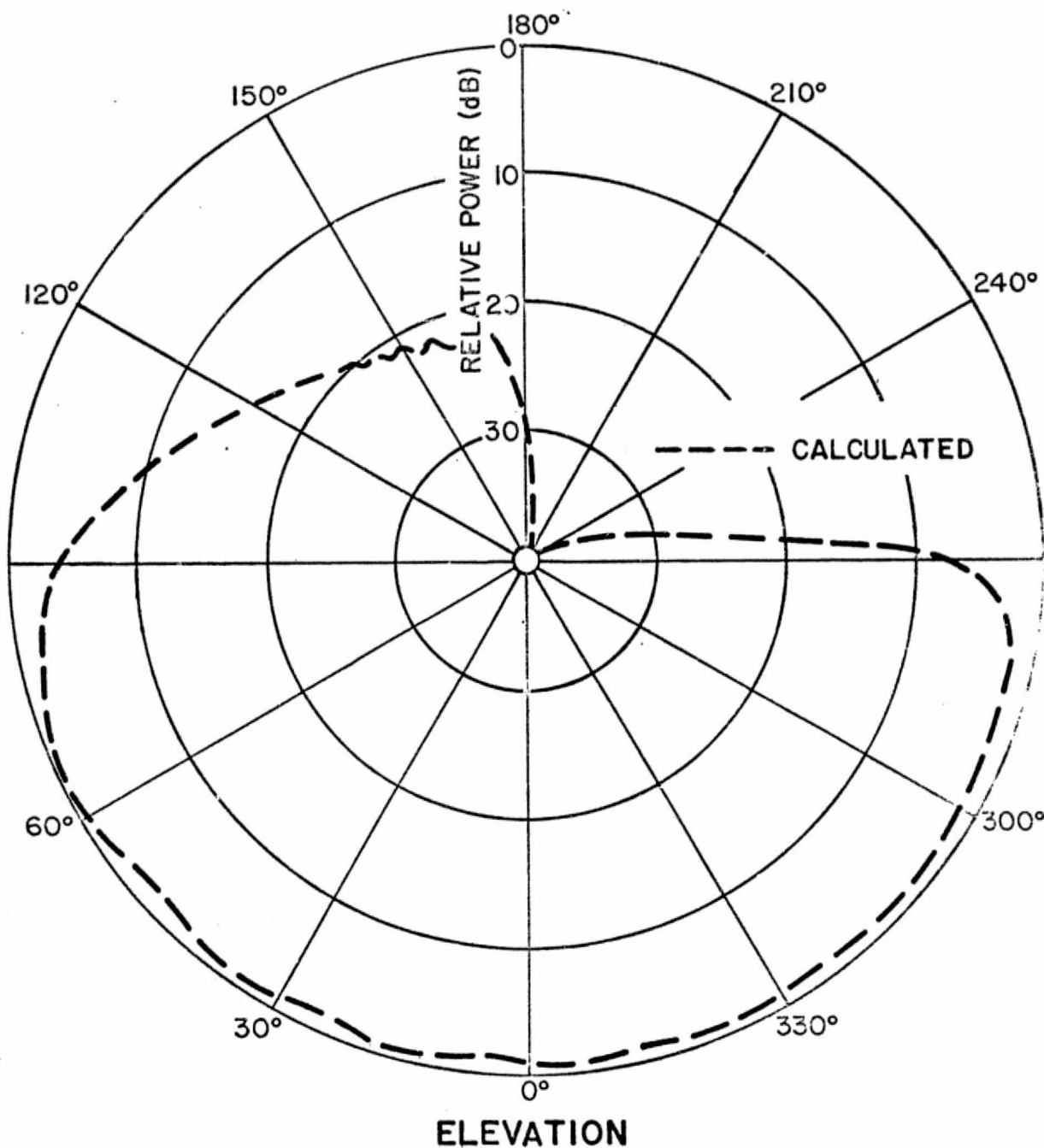Fig. 17c.   Phase error plot of monopole on B-15
aircraft.

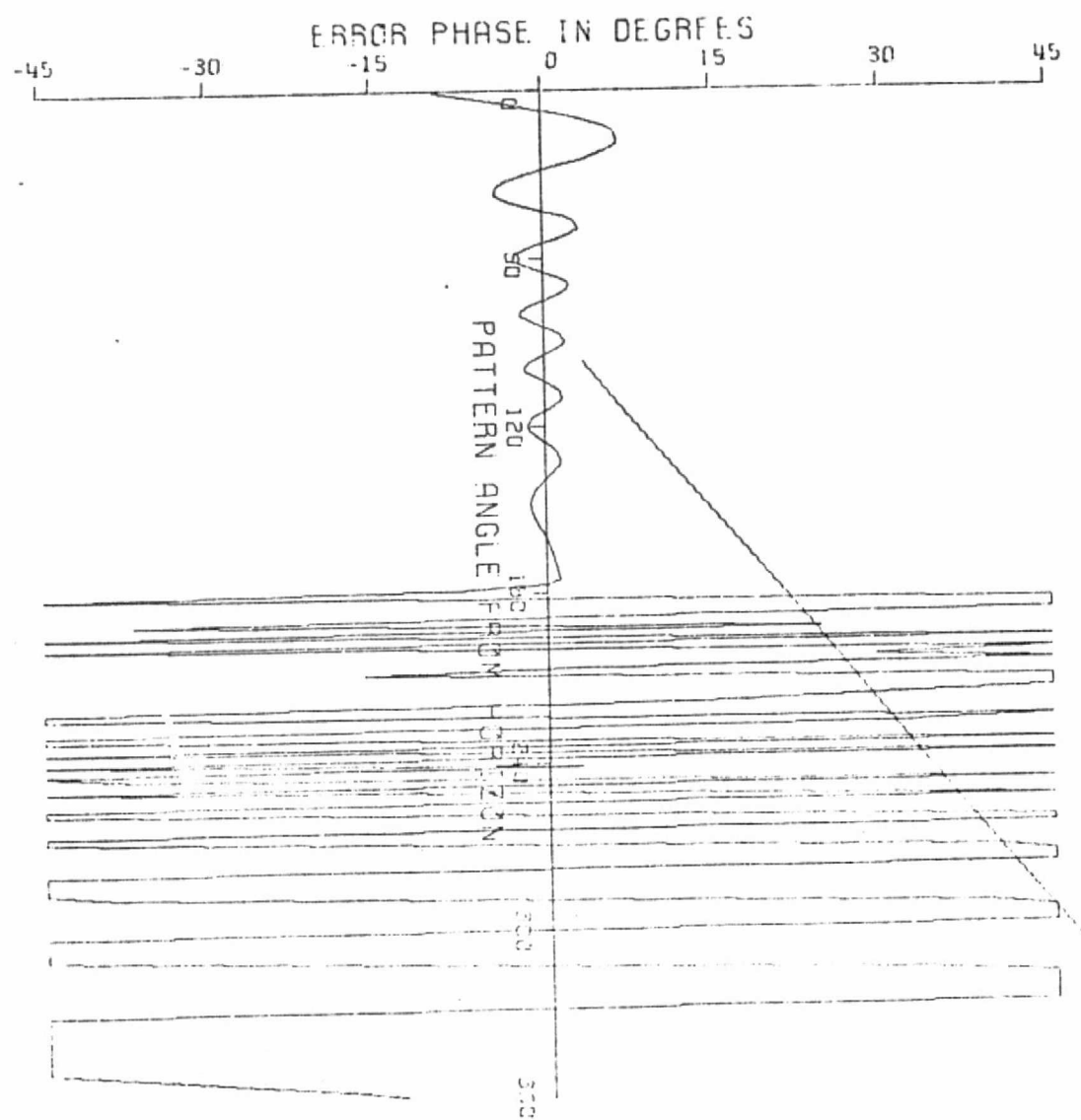Fig. 17d. Elevation pattern of circumferential slot of B-15 aircraft.

Fig. 17e. Phase error plot of circumferential slot
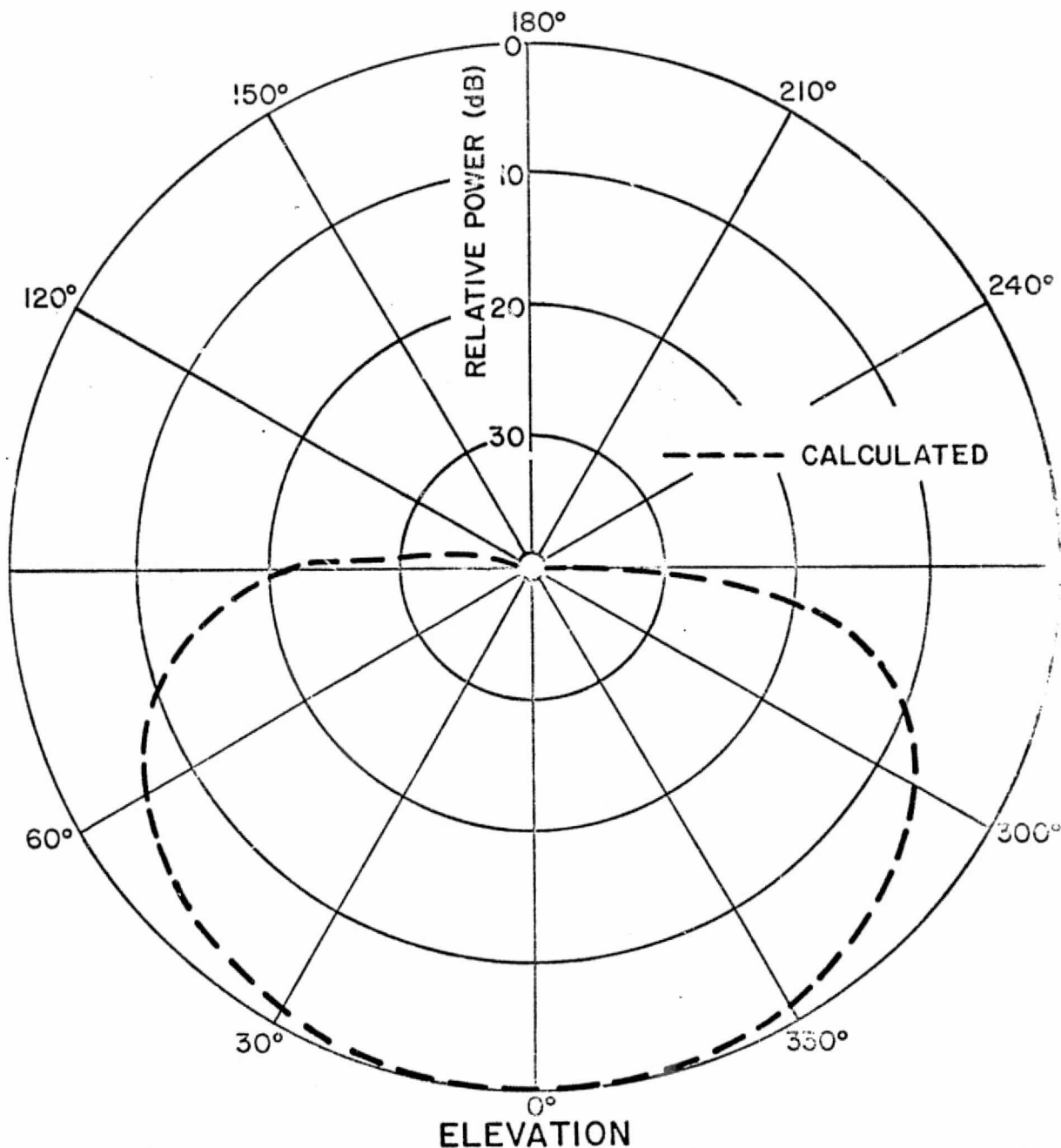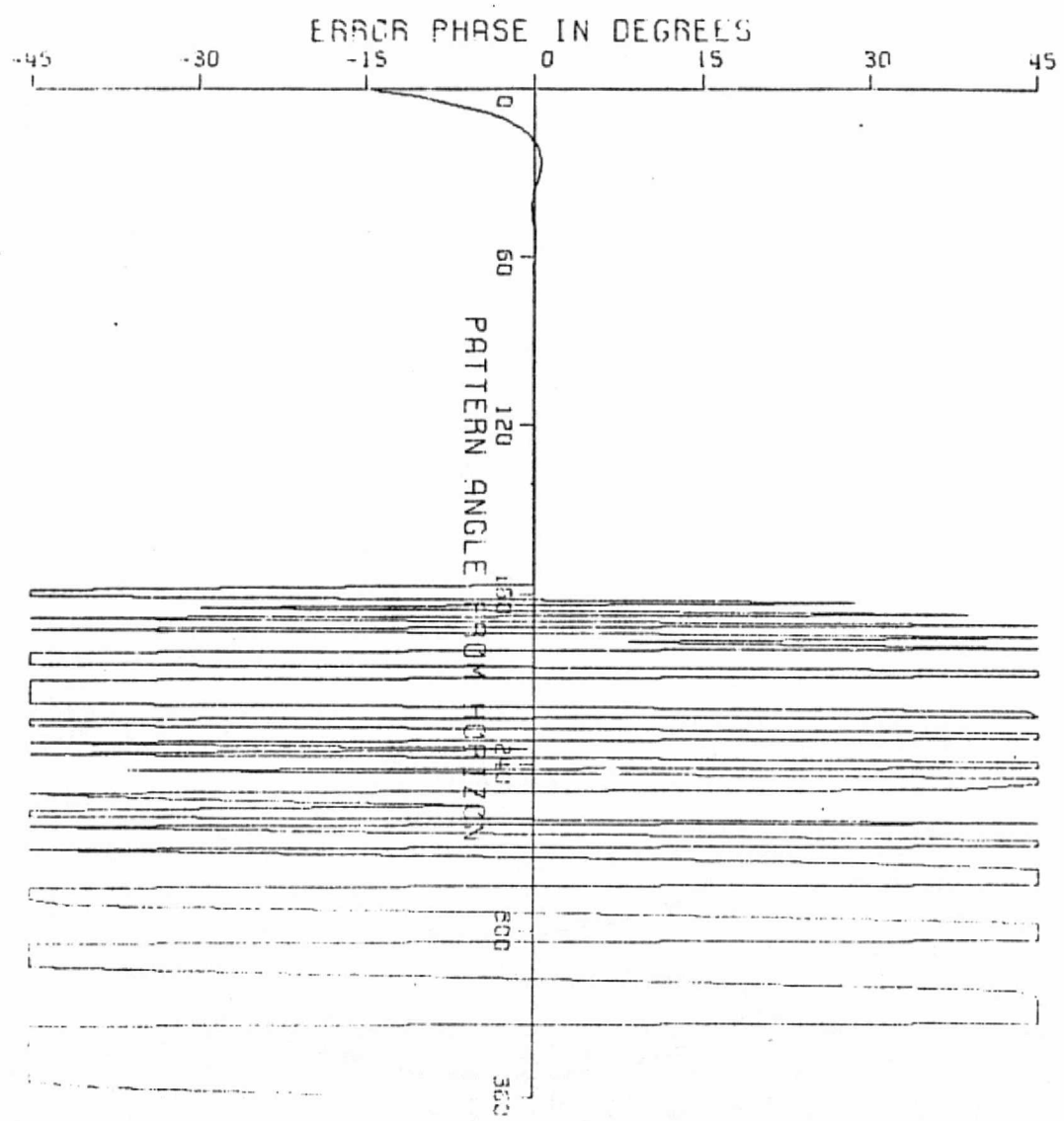of B-15 aircraft.

50

HORIZONTA POL.
SLOT

Fig. 17f.   Elevation pattern of axial slot of B-15
aircraft.

51

Fig. 17g.   Phase error plot of axial slot of B-15
            aircraft.

52

REFERNCES

1. J. B. Keller, "Geometrical Theory of Diffraction," J. Opt. Soc. Am., Vol. 52, No. 2, February 1962, pp. 116-130.

2. R. C. Rudduck, "Application of Wedge Diffraction to Antenna Theory," Report 1691-13, 30 June 1965, ElectroScience Laboratory, Department of Electrical Engineering, The Ohio State University; prepared under grant NsG-448, for National Aeronautics and Space Administration.

3. Prabhaker H. Pathak and Robert G. Kouyoumjian, "An Analysis of the Radiation from Apertures in Curved Surfaces by the Geometrical Theory of Diffraction," IEEE Proceedings, Vol. 62, No. 11, November 1974.

4. W. D. Burnside, "Analysis of On-Aircraft Antenna Patterns," Report 3390-1, August 1972, ElectroScience Laboratory, Department of Electrical Engineering, The Ohio State University; prepared under Contract N62269-72-C-0354 for Naval Air Development Center. (AD 777989)

5. W. D. Burnside, M. C. Gilreath, R. J. Marhefka, and C. L. Yu, "A Study of KC-135 Aircraft Antenna Patterns," IEEE Trans. on Antennas and Propagation, Vol. Ap-23, No. 3, May 1975, pp. 309-16.

6. W. D. Burnside, R. J. Marhefka, and C. L. Yu, "Roll-Plane Analysis of On-Aircraft Antennas," IEEE Trans. on Antennas and Propagation, Vol. Ap-21, No. 6, November 1973, pp. 780-86.

7. W. D. Burnside, C. L. Yu, and R. J. Marhefka, "Flush-Mounted Antennas Radiating Through Dielectric-Covered Curved Surfaces," Report 3001-5, July 1973, ElectroScience Laboratory, Department of Electrical Engineering, The Ohio State University; prepared under Grant No. NGR 36-008-144 for National Aeronautics and Space Administration, Langley Center. (NASA-CR-2403) (N74-28707)

8. Y. M. Hwang and R. G. Kouyoumjian, "A Dyadic Diffraction Coefficient Coefficient for an Electromagnetic Wave which is Rapidly-Varying at an Edge," presented at URSI Meeting, Boulder, Colorado, October 1974.

9. P. H. Pathak and R. G. Kouyoumjian, "The Dyadic Diffraction Coefficient for a Perfectly-Conducting Wedge," Report 2183-4, 5 June 1970, ElectroScience Laboratory, Department of Electrical Engineering, The Ohio State University; prepared under Contract AF 19(628)-5959 for Air Force Cambridge Research Laboratory. (AFCRL-69-0412) (AD 707827)